Economic Geology, v. 104, pp. 73–93

Sediment-Hosted Gold Deposits in Guizhou, China: Products of Wall-Rock Sulfidation by Deep Crustal Fluids

Wenchao Su,†

State Key Laboratory of Ore Deposit Geochemistry, Institute of Geochemistry, Chinese Academy of Sciences, Guiyang 550002, China, and Key Laboratory of Marginal Sea Geology, Guangzhou Institute of Geochemistry, Chinese Academy of Sciences, Guangzhou 510640, China

Christoph A. Heinrich,

Isotope Geochemistry and Mineral Resources, Department of Earth Sciences, Swiss Federal Institute of Technology, ETH Zentrum CH-8092 Zürich, Switzerland, and Faculty of Mathematics and Natural Sciences, University of Zürich, Switzerland

Thomas Pettke,*

Isotope Geochemistry and Mineral Resources, Department of Earth Sciences, Swiss Federal Institute of Technology, ETH Zentrum CH-8092 Zürich, Switzerland

Xingchun Zhang, Ruizhong Hu,

State Key Laboratory of Ore Deposit Geochemistry, Institute of Geochemistry, Chinese Academy of Sciences, Guiyang 550002, China

and Bin Xia

Key Laboratory of Marginal Sea Geology, Guangzhou Institute of Geochemistry, Chinese Academy of Sciences, Guangzhou 510640, China

Abstract

Sediment-hosted gold deposits in Guizhou, China, are hosted in late Paleozoic and early Mesozoic sedimentary rocks along the southwest margin of the Precambrian Yangtze craton. They have characteristics similar to Carlin-type gold deposits in Nevada and are notably enriched in As, Sb, Hg, and Tl. The Shuiyindong and Yata deposits consist of disseminated, strata-bound sulfides in Permian bioclastic limestone and fault-controlled mineralization in Middle Triassic calcareous clastic rocks, respectively. Mineralization in both deposits consists of barren milky quartz veins, disseminated gold-bearing arsenian pyrite and arsenopyrite, stibnite, realgar, and orpiment. The barren milky quartz veins occur in the ore-controlling structures with an envelope of gold mineralization in the host rock consisting of disseminated gold-bearing arsenian pyrite and arsenopyrite and replacement-style quartz veinlets. Later drusy quartz, stibnite, realgar, and orpiment fill fractures and vugs on the periphery of gold mineralization. Petrography, microthermometry, laser Raman spectroscopy, and laser ablation inductively coupled plasma mass spectrometric (LA-ICP-MS) analyses of fluid inclusions are used to characterize the chemical evolution of ore fluids at Shuiyindong and Yata.

Early barren milky quartz veins trapped aqueous fluid with moderate salinity (6.0 wt % NaCl equiv) and minor CO_2 (<2.4 mol %) at a temperature of 230° ± 30°C. This fluid contains measurable B, Na, K, Cs, Sr, As, Sb, and Au (3.8 ± 0.5–5.7 ± 2.3 μg/g) determined by LA-ICP-MS and is interpreted to approximate the mineralizing fluid responsible for precipitation of early barren quartz veins. Low-salinity (0.9–2.3 wt % NaCl equiv), CO_2-bearing (6.3–8.4 mol %), aqueous fluids are recorded in replacement-style quartz veinlets. They formed gold-bearing arsenian pyrite and arsenopyrite and quartz veinlets at a temperature of 210° ± 20°C and pressures of 450 to 1,150 bars, corresponding to depths between 1.7 and 4.3 km under lithostatic conditions. Fluid inclusions in late stibnite-orpiment-realgar-quartz veins contain high CO_2 (58–64 mol %) and N_2 (19.2–23.7 mol %) with trace CH_4 (up to 1.6 mol %). The increasing content of CO_2 and decrease in the concentrations of Au and As in aqueous-carbonic inclusions are interpreted to result from carbonate dissolution at the level of the deposits during gold mineralization. Covariance of Au, As, Sb, and Sr concentrations in the fluids is interpreted to reflect deposition of As and Sb sulfides and gold concurrent with carbonate crystallization. Iron is below detection limit (~400 μg/g) in all fluid inclusion types, suggesting that the ore fluids were Fe poor but possibly sulfur rich, possibly explaining their exceptionally high gold contents. Iron in sulfide minerals was probably derived from dissolution of ferroan minerals in the host rocks, sulfidized by H_2S-rich fluids to precipitate arsenian pyrite, arsenopyrite, and gold. Pressure fluctuation induced by faulting resulted in local fluid immiscibility and led to late deposition of realgar, orpiment, stibnite, and calcite.

Hydrogen and oxygen isotope compositions of ore fluids ($\delta D_{(H_2O)}$ = –35 to –68‰, $\delta^{18}O_{(H_2O)}$ = 4–16.5‰) indicate a metamorphic origin, possibly related to crustal thickening and prograde metamorphism during the late Yanshanian orogeny.

† Corresponding author: e-mail, suwenchao@vip.gyig.ac.cn
*Present address: University of Bern, Baltzerstr. 1-3, CH-3012 Bern, Switzerland.

Introduction

SEDIMENT-HOSTED gold deposits in Guizhou, China, are hosted in late Paleozoic and early Mesozoic sedimentary rocks along the southwest margin of the Precambrian Yangtze craton. They have characteristics similar to Carlin-type gold deposits in Nevada, including notable enrichment in As, Sb, Hg, and Tl (Hu et al., 2002; Peters et al., 2007). Most deposits are strata bound and/or fault controlled (Zhang et al., 2003; Peters et al., 2007). The strata-bound mineralization is controlled by anticlines and is hosted in Permian bioclastic limestone (e.g., Shuiyindong). The fault-controlled mineralization occurs along compressive shear zones in Middle or Lower Triassic siltstone and silty mudstone (e.g., Yata). Typical characteristics include impure carbonate or calcareous and carbonaceous host rock that contains disseminated pyrite and arsenopyrite. Gold occurs either as submicrometer-sized particles or invisibly as solid solution in As-rich rims of pyrite and arsenopyrite (Mao, 1991; Zhang et al., 2005; Su et al., 2008). Late stibnite, realgar, and orpiment fill fractures on the periphery of gold mineralization. Hydrothermal alteration caused decarbonation, silicification, argillization, and sulfidation (Hu et al., 2002; Zhang et al., 2003; Su et al., 2008), similar to Carlin-type gold deposits in Nevada (Hofstra et al., 1991; Arehart, 1996; Hofstra and Cline, 2000; Emsbo et al., 2003; Kesler et al., 2003).

The physical and chemical characteristics of the ores are well constrained for Carlin-type deposits in both the United States and China. Sulfidation is recognized to be the most important mechanism of gold deposition, whereby gold and pyrite precipitated together from H_2S-rich fluids that reacted with Fe minerals in the host-rock package (Hofstra et al., 1991; Hofstra and Cline, 2000; Kesler et al., 2003). However, the source and evolution of ore fluids in Carlin-type systems remain a contentious issue (Cline and Hofstra, 2000), partly because the root of the ore-fluid system is difficult to identify. In the Shuiyindong and Yata deposits, quartz crystals in veins or stockworks associated with mineralization are somewhat coarser than those in most Carlin-type gold deposits. Fluid inclusions in the coarser quartz crystals are commonly 20 μm in diameter or larger and have clear paragenetic relationships of entrapment. These have been used to characterize the P-V-T-X evolution of fluids responsible for Carlin-type gold mineralization in the Shuiyindong and Yata deposits, by combining detailed petrography, microthermometry, and laser Raman spectroscopy with laser ablation inductively coupled plasma mass spectrometric (LA-ICP-MS) analysis.

Regional Geologic Setting

Carlin-type gold deposits in the southwestern Guizhou (Fig. 1) lie near the southwestern margin of the Yangtze craton, which is composed of Proterozoic low-grade metamorphic rocks overlain by thick carbonate and shale sequences of Cambrian to Triassic age (Wang et al., 1995). The outcropping strata in the area are mostly Permian and Triassic, with the Permian rocks generally exposed in the cores of anticlines. The rocks consist of limestone, dolomite, siltstone, sandstone, and shale of shallow- and deep-water facies. From the northwest to the southeast, the sedimentary environment gradually changes from continental and shallow-water platform to deep water in the Youjiang rift basin. The basin margin formed in the Devonian during opening of the Paleo-Tethys (Liu et al., 2002). Most of the sedimentary rocks in the Youjiang basin have illite crystallinities indicative of low-grade burial metamorphism (anchi- to epizone: Suo et al., 1998).

Between the Middle Triassic and Early Jurassic, southwestern Guizhou was in a foreland fold- and -thrust setting on the northwest side of the Yanshanian orogen (Li and Li, 2007). The basin sequence was folded and uplifted by the orogeny as the Pacific plate was subducted beneath the Eurasian plate (Hu et al., 2002). The intensity of deformation caused by the orogenic event was highly variable (Wang et al., 1995). The Permian and Triassic carbonate and clastic platform facies were gently folded or domed and exhibit brittle deformation. Deep basin rocks affected by the orogenic event to the southeast (e.g., in the vicinity of Yata) have been tightly folded resulting in high-angle ductile-brittle reverse faults.

Granites and felsic volcanic rocks associated with the Yanshanian orogeny occur mainly in eastern China, far from the Carlin-type gold deposits. No felsic intrusive rocks were observed in the southwestern Guizhou or in the vicinity of the gold deposits. Small alkaline ultrabasic pipes and dikes cut Lower Permian to Middle Triassic strata, but well away from known gold deposits, along a north-south–trending transitional sedimentary facies belt; an inferred Puding-Ceyang deep fault may have provided pathways for their emplacement (Fig. 1). The primary mineralogy of the dikes is obscured by alteration and weathering, except for relics of biotite and pyroxene. The least altered biotite was dated at 85.0 ± 0.2 Ma ($^{40}Ar/^{39}Ar$: Su, 2002). It may be interpreted as the onset of extension in response to the Yanshanian orogeny. The oldest volcanic rock, which only crops out in the northwestern part of the area, is alkaline flood basalt of Late Permian age (Emeishan Basalt; Fig. 1). The flood basalts are highly variable in thickness and, generally, do not extend into the area of gold deposits.

The Carlin-type gold deposits in the southwestern Guizhou are hosted in both shallow- and deep-water facies sedimentary rocks of Permian and Triassic age (Fig. 1). Two styles of ore geometry have been recognized. Strata-bound mineralization is controlled by anticlines or domes with ore hosted in Permian bioclastic limestone (e.g., Zimudang and Shuiyindong deposits). Fault-controlled mineralization occurs mainly along reverse faults on the flanks of anticlines or domes, with ore hosted in siltstone and silty mudstone of Middle or Lower Triassic age (e.g., Lannigou and Yata deposits). The age of gold mineralization in the southwestern Guizhou is poorly constrained because of the lack of minerals suitable for isotopic dating. However, fission-track ages on quartz from pyrite-quartz veins in the Lannigou and Baidi deposits are between 82 ± 8 and 91 ± 6 Ma (Zhang and Yang, 1993). Recently, Su et al. (2009) reported Sm-Nd isochron ages of hydrothermal calcite veins coeval with gold mineralization at the Shuiyindong deposit, ranging from 134 ± 3 to 136 ± 3 Ma. Field observations suggest that bedding-parallel or reverse faults, which are important hosts for gold mineralization, were formed during the late stage of the Yanshanian orogeny (140–75 Ma: Hu et al., 2002), an important tectonic event in southeastern China. Therefore, it is reasonable to conclude that gold mineralization in

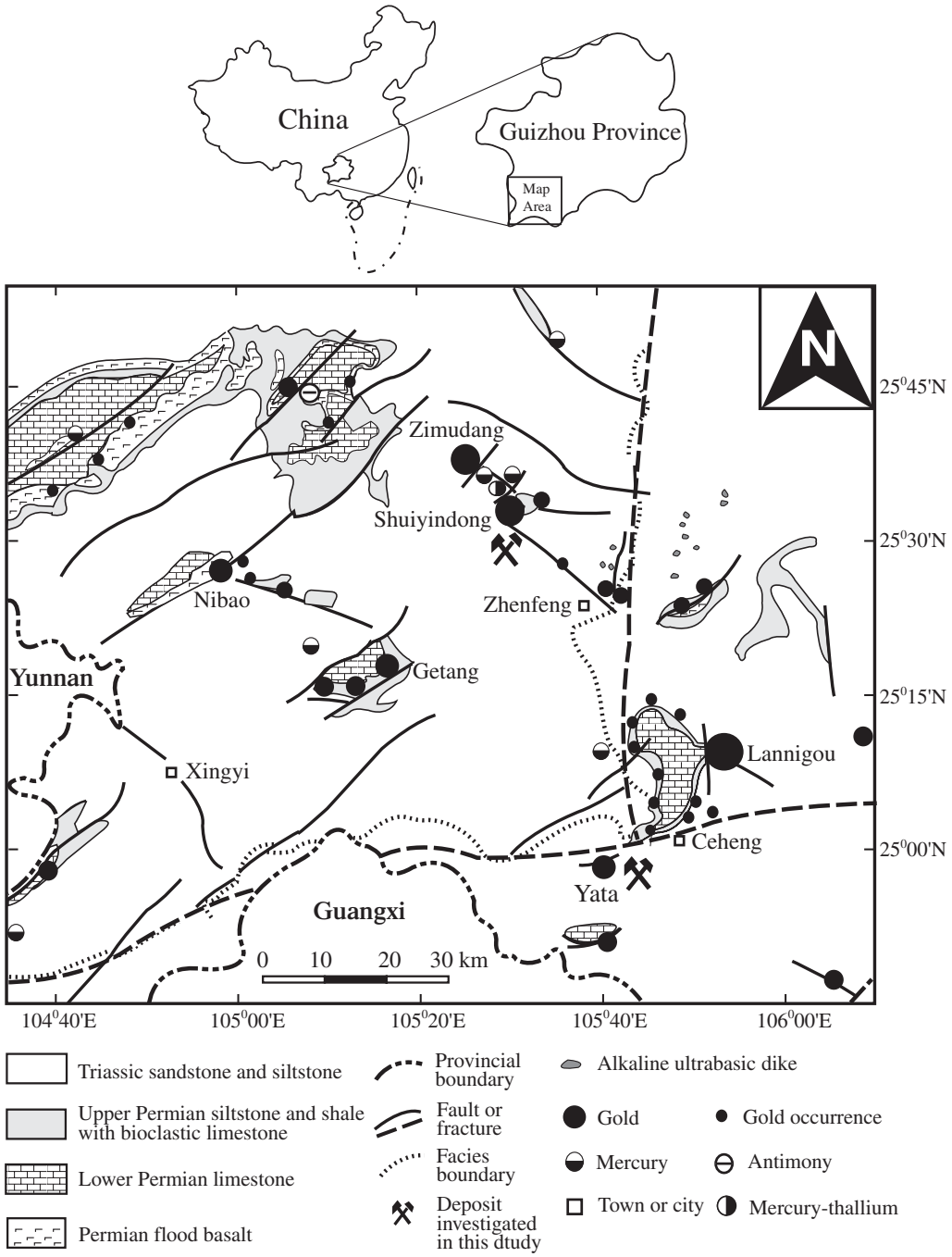

FIG. 1. Simplified geologic map of southwestern Guizhou (modified after Zhang et al., 2003), showing the locations of the major Carlin-type gold (e.g., Shuiyindong and Yata) and antimony and mercury deposits.

Guizhou probably took place during the Late Jurassic to Cretaceous.

Geology of the Shuiyindong and Yata Deposits

Shuiyindong

The Shuiyindong deposit is located about 20 km northwest of the town of Zhenfeng in southwestern Guizhou (Fig. 1). It lies on the eastern limb of the Huijiabao anticline (Fig. 2A), which also hosts a cluster of deposits on its western limb, including the Zimudang deposit. Recent exploration and mining at Shuiyindong has proven gold reserves of 55 metric tons (t) Au (1.8 Moz), with average gold grades from 7 to 18 g/t (Xia, 2005). All of the gold is refractory, occurring in arsenian pyrite and arsenopyrite (Su et al., 2008). The following geologic description of the deposit is from Su et al. (2008).

Sedimentary rocks in the district consist of bioclastic limestone, siltstone, and argillite of the Middle and Upper Permian and Lower Triassic. The Middle Permian Maokou Formation, a massive bioclastic limestone, is overlain by the

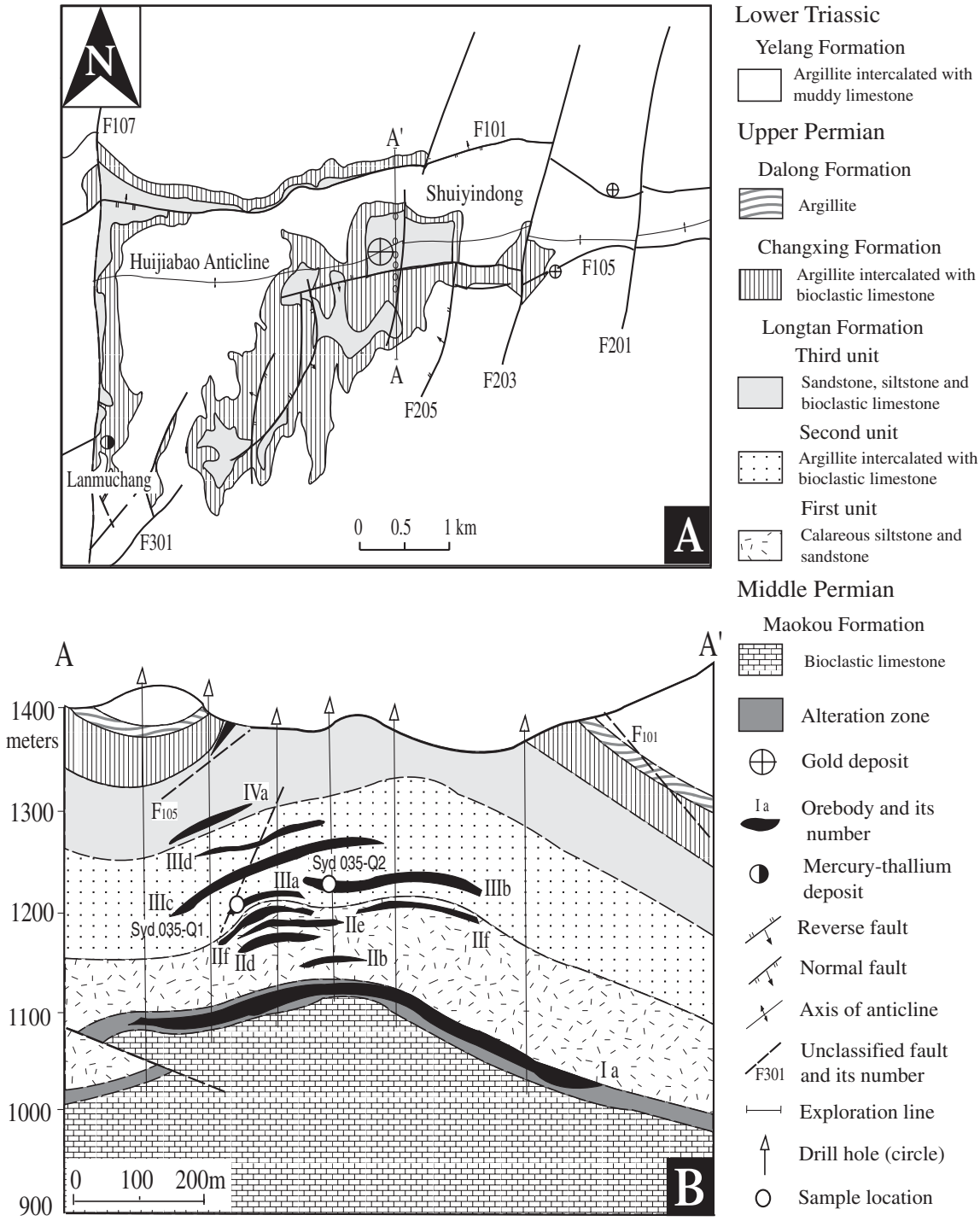

FIG. 2. Simplified geologic plan (A) and cross section (B) along the A-A' exploration line of Shuiyindong (modified from Liu, 2001). Note the stratiform nature of the numbered orebodies.

Upper Permian Longtan, Changxing, and Dalong and Lower Triassic Yelang Formations. The Longtan Formation is about 300 m thick in the Shuiyindong district and has been divided into three stratigraphic units (Liu, 2001). The lowest unit consists of calcareous siltstone, which grades into fine-grained sandstone at the top. The second unit consists of silty argillite intercalated with bioclastic limestone and coal seams. The third unit includes calcareous siltstone, sandstone, and muddy and bioclastic limestone. Gold mineralization is preferentially disseminated in bioclastic limestone and calcareous siltstone of the first and second units of the Longtan Formation at depths of 100 to 300 m below the surface (Fig. 2B). These rocks were deformed into an east-trending anticline with limbs that dip 10° to 20°. Strata-bound gold orebodies

are located mainly on the flanks of the anticline (Fig. 2B). The limbs of the anticline are cut by reverse faults F_{101} and F_{105}, respectively, which strike east-west and dip steeply to the north and south, respectively (Fig. 2A). The reverse faults host small orpiment and realgar bodies with low-grade gold mineralization and are cut by a series of near north-south–trending normal faults with steep dips (70°–80°). The normal faults contain mercury-thallium deposits, such as Lanmuchang (Fig. 2A).

The three main orebodies at Shuiyindong (IIIa, IIIb, IIIc; Fig. 2B) contain approximately half of the gold reserves. They are 100 to 400 m long, 50 to 350 m wide, 1.7 to 1.9 m thick, and have an average gold grade of 16 g/t (Xia, 2005). A lower grade orebody (Ia) is hosted in silicified, brecciated argillite and limestone at the unconformity between the Maokou Limestone and the first unit of the Longtan Formation. This unconformity controlled the distribution of other gold deposits regionally in the southwestern Guizhou, such as Getang and Nibao (Fig. 1), suggesting that it may have been a feeder conduit for gold mineralization. In these orebodies, milky quartz veins are frequently observed and occur nearly as horizontal dips (Fig. 3A). Some of the milky quartz veins are cut by stibnite-realgar-orpiment-quartz veinlets, suggesting that they formed later than the As-Sb mineralization but possibly predated the deposition of the bulk of disseminated gold-bearing arsenian pyrite and arsenopyrite in the host rock.

Wall-rock alteration at Shuiyindong caused decarbonation, silicification, sulfidation, and dolomitization. Decarbonation of limestone is evident from small relict inclusions of calcite and dolomite in jasperoidal quartz (cf. Hofstra and Cline, 2000). Small amounts of gold-bearing arsenian pyrite and arsenopyrite are enclosed within Fe-poor dolomite (Fig. 3C), whereas large amounts of gold-bearing arsenian pyrite and arsenopyrite have grown between quartz and dolomite (Fig. 3D) or enclosed in jasperoidal quartz (Fig. 3E). Sulfides in the deposit consist mainly of arsenian pyrite, arsenopyrite, marcasite, and small amounts of orpiment, realgar, and stibnite. Gangue minerals are quartz, dolomite, calcite, and clay minerals (e.g., kaolinite). The dominant gold-bearing sulfides are arsenian pyrite and arsenopyrite. Arsenian pyrite formed earlier than arsenopyrite in the paragenetic sequence because arsenopyrite occurs as overgrowths on arsenian pyrite. Arsenian pyrite that contains significant gold typically occurs as tiny, irregular grains, generally less than 50 μm in size. Commonly, arsenian pyrite also forms rims on early pyrite crystals (e.g., Zhang et al., 2005, fig. 2e). The core of some early pyrite has a "porous" appearance, possibly owing to conversion of marcasite to pyrite (cf. Murowchick, 1992). Modal analyses showed that the dominant form of gold is "invisible" gold in iron sulfides (95%), with subordinate free native gold (5%; Liu, 2003). Electron microprobe analyses (EMPA) showed that gold is predominantly in arsenian pyrite (400–3,800 ppm Au, 3.37–14.06 wt % As: Su et al., 2008), with lesser amounts in arsenopyrite (300–1,500 ppm Au: Zhang et al., 2008). Lower resolution LA-ICP-MS analyses of arsenian pyrite and arsenopyrite in ore-grade samples from Shuiyindong yielded an average of 200 to 500 ppm Au and demonstrated that Au is associated with As, Sb, Tl, Cu, Pb, Co, and Ni, in decreasing order of correlation (Zhang et al., 2005). A few native gold grains were observed by Su et al. (2008). They occur in arsenian pyrite disseminated in the host rocks and in an arsenian pyrite veinlet (Fig. 3G, H). The size of these native gold grains ranges from 0.1 to 6 μm in diameter. Most are present at the edge of arsenian pyrite crystals in veinlets (Fig. 3G) and some occur in calcite (Fig. 3H), suggesting that ore fluids at Shuiyindong were locally saturated with gold (Su et al., 2008).

Yata

The Yata gold deposit is located about 15 km southwest of the town of Ceheng in southwestern Guizhou (Fig. 1). The deposit had been mined for arsenic (realgar) at a small scale for many years. Gold mineralization was discovered as a result of reconnaissance sampling around the old realgar pits in the early 1980s. Intensive exploration was carried out by the Guizhou Bureau of Geology and Mineral Resources in the late 1980s. This resulted in the definition of more than 10 t of gold reserves, with an average gold grade of 3 to 5 g/t (Tao et al., 1987). Geologic descriptions of the deposit were given by Cunningham et al. (1988), Ashley et al. (1991), and Zhang et al. (2003).

Sedimentary rocks exposed in the district are mainly siltstone, sandstone, argillaceous limestone, and shale of the Middle Triassic Xuman Formation, which is divided into four members based on sand grain size and bedding thickness (Tao et al., 1987). Gold mineralization occurs in Member 2, which is composed of interbedded sandstone, fine-grained sandstone, siltstone, and mudstone. Unmineralized carbonaceous shale in this formation contains quartz, biotite, ferroan dolomite, illite, calcite, and minor fine-grained diagenetic pyrite (Ashley et al., 1991).

Gold mineralization (Fig. 4) occurred along a narrow east-trending zone and comprises more than 40 orebodies (Han et al., 1999). Most of them occur along high-angle and strike-slip faults that cut the south limb of the east-trending Huangchang anticline and subsidiary folds. Limbs of the anticline dip at 35° to 70°, contain chevron folds and mesoscopic compressive fracture zones. Faults F_1, F_2, F_3, and F_6 controlled mineralization within the zone. The F_2 and F_3 faults, which have easterly trends and dip south at 65° to 85°, controlled the largest mineralization zone (M_1) in the district. The M_1 zone is 1,500 m long, 40 to 60 m wide, and 200 m thick, with average gold grades varying from 1 to 3 g/t (Zhang et al., 2003). Smaller orebodies with average gold grades of 3 to 5 g/t occur as lenticular zones, veins, and vein stockworks within the larger envelope of mineralization. Gold orebodies are preferentially hosted in altered calcareous siltstone and shale at intersections with high-angle faults that focused fluid flow during gold mineralization.

Despite the stronger structural control than at Shuiyindong, wall-rock alteration at Yata is similar and extends well away from faults and fractures along more reactive or permeable clastic strata or calcareous shale and siltstone. Carbonate dissolution mostly occurred in carbonate strata. In proximal zones of carbonate dissolution, disseminated irregular or euhedral crystals of orpiment or realgar formed locally in porous decarbonated rocks. Silicification typically produced small bodies of jasperoidal quartz within the larger areas of altered rocks (Fig. 3I). Coarser quartz crystals occur in veins and

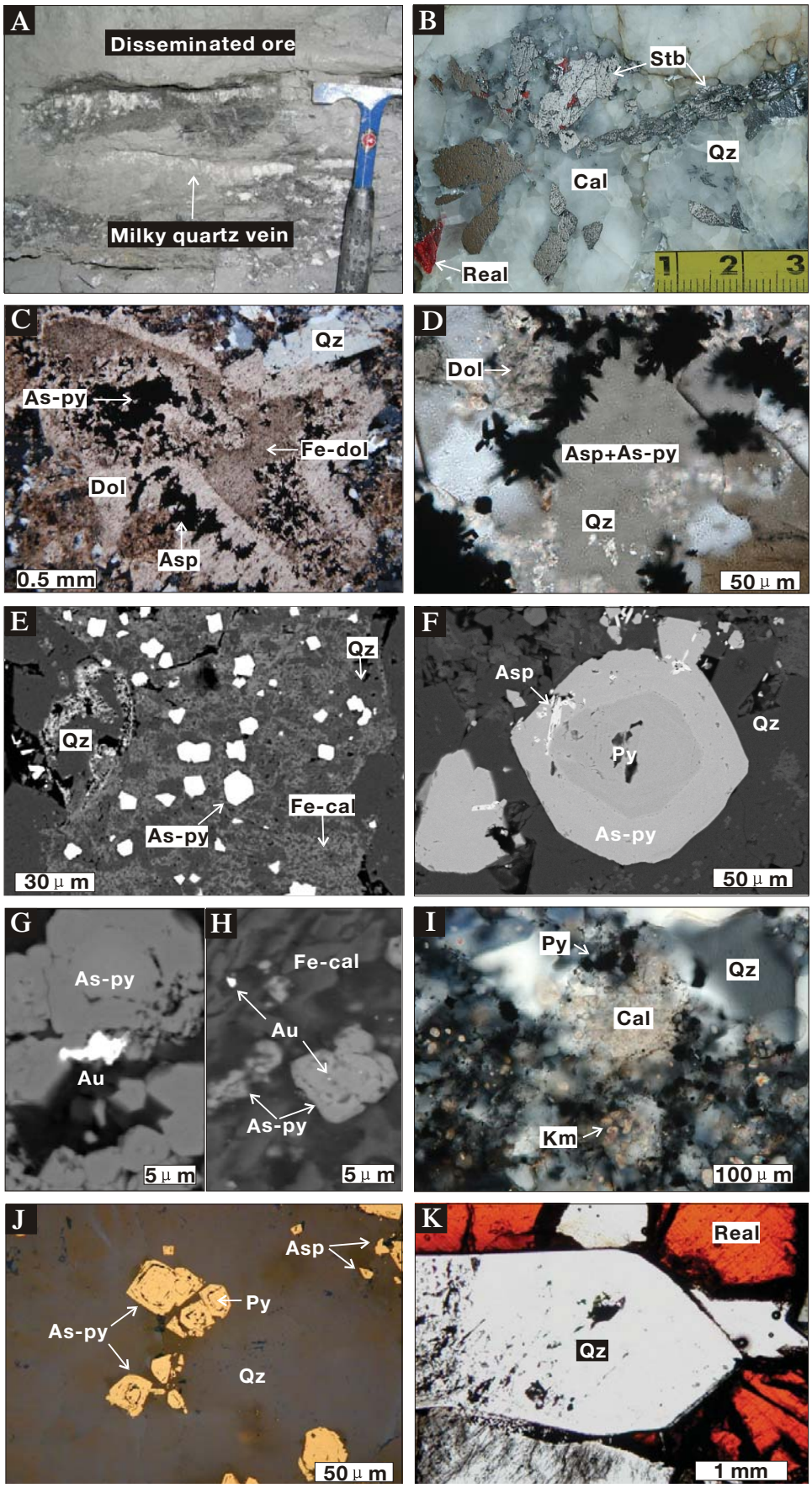
A
Disseminated ore
Milky quartz vein
B
Stb
Qz
Cal
Real
1 2 3
C
Qz
As-py
Fe-dol
Dol
Asp
0.5 mm
D
Dol
Asp+As-py
Qz
50 μm
E
Qz
Qz
Fe-cal
As-py
30 μm
F
Asp
Qz
Py
As-py
50 μm
G
As-py
Au
5 μm
H
Fe-cal
Au
As-py
5 μm
I
Py
Qz
Cal
Km
100 μm
J
Asp
Py
As-py
Qz
50 μm
K
Real
Qz
1 mm

veinlets (Fig. 3J, K). Quartz in the jasperoid has reticulate or xenomorphic textures, variable grain sizes, and abundant small calcite or dolomite inclusions (Fig. 3I), suggesting that it may have formed at moderate temperatures and at greater depths (cf. Hofstra and Cline, 2000). More intense, pervasive silicification generally affected the coarser sandstone where it occurs close to feeder structures. Argillization has mainly produced illite or illite-quartz veinlets, many of which contain pyrite and arsenopyrite.

The dominant primary ore minerals at Yata are arsenian pyrite, arsenopyrite, marcasite, stibnite, orpiment, and realgar (Zhang et al., 2003). Trace amounts of sphalerite, galena, and chalcopyrite also occur. Gangue minerals include quartz, dolomite, calcite, and clay minerals (e.g., illite). Pyrite is the dominant sulfide in the ores (3–5 vol %). It occurs disseminated in the host rocks as rounded pentagonal, dodecahedral, octahedral, and cubic crystals, or as aggregates of all morphologies. Bulk analysis of pyrite has an average gold content of 83 ppm (Han et al., 1999) and arsenic contents of 1 to 7 wt percent (Ashley et al., 1991). EMPA showed that gold is predominantly in arsenian pyrite (540 ppm Au, 10.73 wt % As: Ye et al., 1994), but a few gold grains (0.3–0.8 μm) have been observed in arsenian pyrite using scanning electron microscopy (Ye et al., 1994). Arsenopyrite is generally disseminated in the ore as tiny acicular to prismatic crystals. Some arsenopyrite occurs as rims on pyrite. Marcasite occurs as rare, tiny grains surrounding pyrite grains. Some stibnite formed early, although later than the gold-bearing pyrite, because stibnite crystals have overgrown on gold-bearing pyrite crystals at their margins. Most of the stibnite formed euhedral crystals filling fractures on the periphery of gold mineralization, local overgrowths of realgar and orpiment (Fig. 3B). Orpiment and realgar are also commonly observed in open cavities with euhedral quartz crystals (Fig. 3K) and fractures in the ore zones or their vicinities. Some calcite-orpiment-realgar veinlets cut pyrite-arsenopyrite-jasperoidal quartz veinlets.

In summary, the occurrence, textures, crosscutting relationships, and mineral assemblages of the ores at Shuiyindong and Yata indicate that ore-bearing minerals were deposited in three hydrothermal stages (Zhang et al., 2003; Hofstra et al., 2005): (1) early-stage milky quartz ± pyrite ± arsenopyrite veins; (2) main-stage vein and replacement-style quartz-dolomite-arsenian pyrite-arsenopyrite; (3) late-stage quartz-calcite ± dolomite-stibnite-orpiment-realgar veinlets. The paragenetic sequence and associated fluid inclusion assemblages are summarized in Figure 5.

Samples and Fluid Inclusion Methods

Eight samples used in this study were collected from the main orebodies in the Shuiyindong and Yata deposits (Figs. 2B, 4B). Three are barren milky quartz veins that have early horizontal dips in the ore zones at Shuiyindong and fill fractures at Yata. Some of the milky quartz veins are colored orange or gray by inclusions of realgar or stibnite or are cut by stibnite-realgar-orpiment-quartz veinlets. A sample (YT-5) from Yata contains arsenian pyrite, arsenopyrite, and quartz (Fig. 3J); other samples from Yata contain stibnite, realgar, orpiment, calcite, and quartz (Fig. 3B, K), filling in fractures on the periphery of gold mineralization.

Doubly polished sample sections, about 200 μm thick, were examined. Fluid inclusion observations were made using a standard optical petrographic microscope and a scanning electron microscope cathodoluminescence (SEM-CL) imaging system to identify successive generations of fluid inclusion-bearing vein quartz and to document its paragenetic relationship to ore minerals. These studies enabled successive assemblages of fluid inclusions to be defined. Representative samples of such assemblages were selected for detailed microthermometric, laser Raman spectroscopic, and LA-ICP-MS studies.

Microthermometric measurements were made on a Linkam THMSG 600 programmable heating-freezing stage mounted on a Leica microscope coupled to an image analysis system at the Institute of Geochemistry, Chinese Academy of Sciences (IGCAS) in Guiyang, China. The equipment was calibrated with melting-point standards (CCl_4, –22.99°C; KNO_3, 333°C) and the melting point of CO_2 (–56.6°C) in synthetic fluid inclusions (Sterner and Bodnar, 1984). Temperature measurements have an uncertainty of about ±0.2° below 50°C and ±2° for temperatures above 100°C. All fluid inclusions were analyzed by cycles of freezing down to –180°C and heating up at rate of 0.2 to 0.5°C/min. Near the melting temperatures of carbonic phase ($T_{m(CO_2)}$) and clathrate ($T_{(m(cl))}$), the heating rate was reduced to 0.1°C/min.

For volatile-rich fluid inclusions, CO_2 was identified by melting of a solid phase in inclusions below –56.6°C. The volumetric fraction of phases in fluid inclusions was estimated at room temperature by reference to the volumetric chart of Roedder (1984), using regular-shaped, flat inclusions whenever possible according to the suggestion of Diamond (2001). Volatile species (e.g., CO_2, CH_4, and N_2) in individual fluid inclusions that are representative of particular populations were

FIG. 3. Examples of ores from Shuiyindong and Yata. A. Photograph of milky quartz veins from Shuiyindong. B. Slab of a quartz vein showing paragenetic relationships among calcite, stibnite, and realgar from Yata. C. Microphotograph (cross-polarized light) of ore from Shuiyindong showing coprecipitated gold-bearing pyrite and arsenopyrite overgrowing Fe-poor dolomite. D. Microphotograph (cross-polarized light) of ore from Shuiyindong showing gold-bearing arsenian pyrite and arsenopyrite between quartz and dolomite on jasperoidal quartz. E. Backscattered electron (BSE) image showing arsenian pyrite disseminated within jasperoidal quartz from Shuiyindong. Note small relict inclusions of ferroan calcite in jasperoidal quartz. F. BSE image of arsenian pyrite in wall rock from Shuiyindong, with As-poor pyrite core overgrown by As-rich rim. G. and H. High magnification BSE images of native gold grains in arsenian pyrite and calcite from Shuiyindong. I. Microphotograph (cross-polarized light) of typical ore from Yata showing intimate intergrowth of gold-bearing pyrite and quartz grains. J. Arsenopyrite- and gold-bearing pyrite crystals with As-rich rims in a quartz vein from Yata (reflected light). K. Late-stage realgar which has overgrown euhedral quartz in a vein from Yata. Abbreviations: Asp = arsenopyrite, As-py = arsenian pyrite, Cal = calcite, Dol = dolomite, Fe-cal = ferroan calcite, Fe-dol = ferroan dolomite, Km = potassium mica, Py = pyrite, Qz = quartz, Real = realgar, Stb = stibnite.

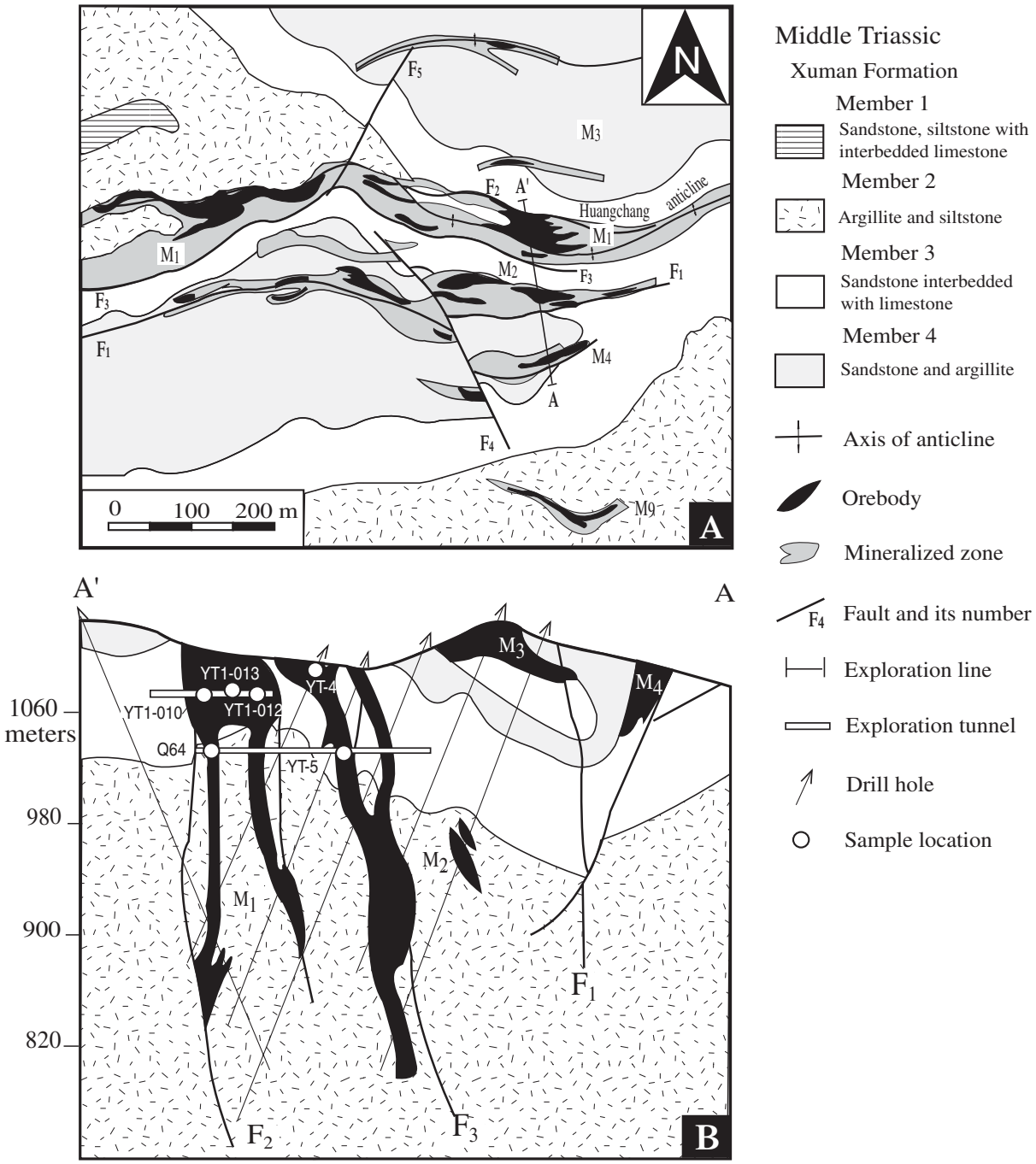

FIG. 4. Simplified geologic plan (A) and cross section (B) along the A-A' exploration line of Yata (after Zhang et al., 2003). Note the vertical (± fault-controlled) orientation of the orebodies.

analyzed by laser Raman spectroscopy, performed on a Renishaw RM 2000 Raman spectrometer at Nanjing University, China. Molar fractions of CO_2, CH_4, and N_2 were determined using the method of Burke (2001).

Salinities expressed as wt percent NaCl equiv were calculated from the final melting temperature of ice in aqueous fluid inclusions according to the method of Bodnar (1993). The salinity of the CO_2-rich inclusions was calculated from the melting temperature of clathrate, using the computer programs of Bakker (1997) based on Diamond (1992). Bulk composition and molar volume were computed based on the P-T-V-X properties of individual inclusions in the C-H-O-N system (Thiéry et al., 1994; Bakker, 1997) using computer programs developed for fluid inclusion studies (Bakker and Brown, 2003). The P-T properties were modeled using the V-X data and the equation of state from Bowers and Helgeson (1983) as revised by Bakker (1999) for aqueous-carbonic fluid inclusions. For carbonic-rich inclusions, the equation of state from Duan et al. (1992, 1996) for the C-H-O-N-S system was applied.

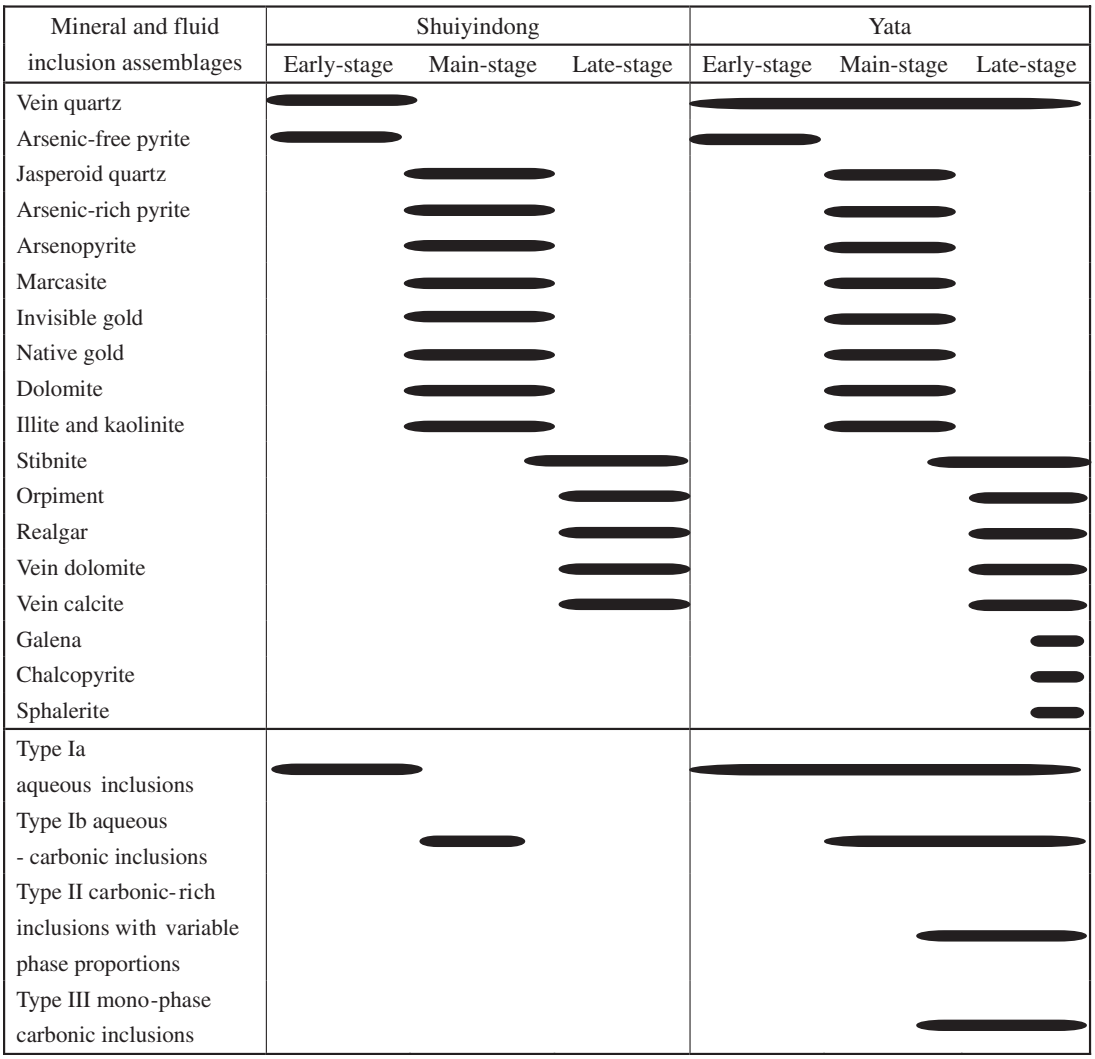

FIG. 5. Paragenetic sequences of minerals and fluid inclusion assemblages at Shuiyindong and Yata, showing essentially similar mineralization history. Two-phase, liquid-rich aqueous inclusions (type Ia) occur in barren milky quartz veins in both deposits. Two- or three-phase aqueous-carbonic inclusions (type Ib) are mainly observed in quartz veinlets at Yata and in jasperoidal quartz with arsenian pyrite and arsenopyrite at Shuiyindong. Two- or monophase carbonic-rich inclusions (type II and III) occur in drusy quartz with realgar, stibnite, and calcite at Yata.

The compositions of fluid inclusions from selected assemblages were analyzed quantitatively by laser-ablation ICP-MS at ETH Zürich, Switzerland. Individual fluid inclusions were opened with a 193-nm Excimer laser (Compex 110 I, ArF, Lambda Physics), and the laser-ablation aerosol was transferred with helium carrier gas into the ICP-MS (ELAN 6100 DRC; Günther et al., 1998; Günther and Heinrich, 1999; Heinrich et al., 2003). ICP-MS conditions were similar to those reported in Pettke et al. (2004). Boron, Na, Mg, K, Mn, Fe, Cu, Pb, Zn, As, Sb, Au, Ag, Sr, Cs, and U concentrations and their detection limits were measured in each inclusion (App.), using SRM 610 from NIST as external standard and data reduction following Heinrich et al. (2003).

Fluid Inclusion Types and Petrographic Relationships

Fluid inclusions observed in this study have negative crystal, elongate, or irregular shapes (Fig. 6). Fluid inclusions types were classified based on their appearance at 25°C and by their Raman spectra and occur in successive stages of the vein and alteration paragenesis, as summarized in Figure 5.

Type Ia inclusions are two-phase, liquid-rich aqueous inclusions with 10 to 20 vol percent of a low-density vapor bubble at room temperature. They occur in early barren milky quartz veins at Shuiyindong and Yata. Primary inclusions of this type occur along growth zones of quartz and have negative crystal shapes, generally less than 25 μm in diameter (Fig. 6B, E). Secondary inclusions are elongate or irregular and occur along trails crosscutting quartz grains or grain boundaries (Fig. 6C, F). Raman spectroscopy analysis has failed to accurately determine the composition of the vapor phase of this type of inclusion because the bubble moved as the laser beam was focused on it. Raman peaks of CO_2, N_2, and CH_4 have, however, been detected.

Type Ib inclusions are two- or three-phase aqueous-carbonic inclusions with a dominant aqueous liquid phase and a relatively constant carbonic (vapor + CO_2 liquid) fraction of

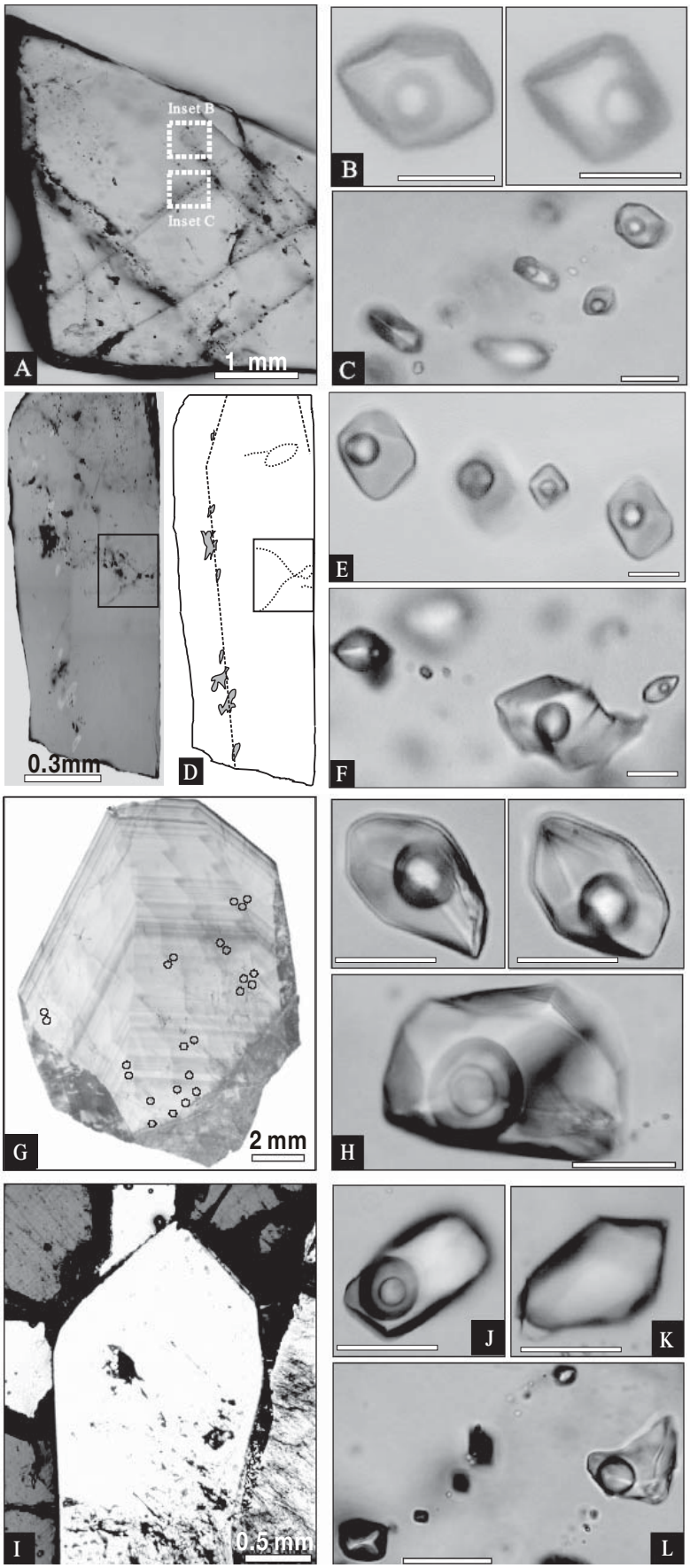
Inset B
Inset C
1 mm
A
B
C
0.3mm
D
E
F
2 mm
G
H
0.5 mm
I
J
K
L

15 vol percent (Fig. 6H). They are commonly observed in quartz veinlets with arsenian pyrite and arsenopyrite of the main stage of gold mineralization at Yata (Fig. 3J) and in jasperoidal quartz of the main stage at Shuiyindong. Primary inclusions are typically 20 μm in diameter, occur along growth zones of quartz, and have negative crystal shapes (Fig. 6G, H). Some inclusions along microfracture planes within quartz grains are pseudosecondary based on their spatial relationship to the growth zones and healed fractures. Both microthermometry and Raman spectroscopy analyses have revealed that the main component of the volatile phase of the inclusions is CO_2, with minor N_2 and trace CH_4.

Type II inclusions are rare, two-phase, aqueous-carbonic inclusions with variably high proportions of a carbonic phase ranging from 45 to 90 vol percent (Fig. 6K). In samples from Yata, they occur in late drusy quartz with realgar, stibnite, and calcite (Fig. 3B, K).

Type III inclusions are monophase carbonic inclusions (Fig. 6L) and generally less than 15 μm in diameter. They are restricted to late quartz-realgar veins or veinlets at Yata and occur along trails crosscutting quartz grains. Both microthermometry and Raman spectroscopy have revealed that the volatile phase is mainly composed of CO_2 and N_2, with trace CH_4.

Petrographic relationships indicate that CO_2-poor aqueous inclusions of type Ia can be interpreted to approximate the mineralizing fluid, which was responsible for precipitation of early ore minerals in veins but predates the deposition of the bulk of disseminated gold-bearing arsenian pyrite and arsenopyrite deposition in both deposits. CO_2-rich fluids of type Ib are interpreted to correspond to the main gold-bearing fluid in both deposits. The same aqueous-carbonic fluids also occur together with type II and III carbonic fluids in the late quartz-realgar veins at Yata. Type II and III fluids are interpreted to represent the waning or outflow stage of economic gold mineralization.

Quantitative Fluid Inclusion Results

Microthermometry and Raman data

Microthermometric measurements were made on primary, pseudosecondary, and secondary inclusions in quartz crystals from milky quartz veins, replacement-style quartz veinlets, and late drusy quartz. Three distinctive fluid compositions are interpreted to be representative of the different mineralization stages. Microthermometric data are summarized in Table 1 and Raman spectroscopy analyses of representative fluid inclusions are given in Table 2.

Type Ia primary and secondary aqueous inclusions (Fig. 6B-C, E-F) have initial ice-melting temperatures (T_e) from –22.2° to –21.0°C, which is similar to the eutectic melting temperature in the NaCl-H_2O system (Hall et al., 1988) but does not exclude more complex systems such as the NaCl-KCl-H_2O system (Sterner et al., 1988). Final ice-melting temperatures (T_m) of primary aqueous inclusions range from –3.0° to –4.3°C, corresponding to salinities of 5.0 to 6.9 wt percent NaCl equiv (Bodnar, 1993) with an average of 6.0 wt percent NaCl equiv (Fig. 7B, D). Homogenization of these fluid inclusions was to the liquid phase at temperatures ranging from 190° to 258°C with a mode around 230°C (Fig. 7A, C). The T_m of secondary inclusions range from –1.2° to –4.5°C, corresponding to salinities of 2.1 to 7.2 wt percent NaCl equiv (Fig. 7B, D). Secondary inclusions of type Ia also homogenized into the liquid phase at temperatures ranging from 151° to 261°C with a mode around 190°C (Fig. 7C). No evidence of other phases, such as clathrate, liquid, or solid CO_2 were observed, suggesting that this type of inclusion may contain as much as 2.4 mol percent CO_2 dissolved in the aqueous phase without developing a separate CO_2 liquid phase at room temperature (Bodnar et al., 1985).

Type Ib primary and secondary aqueous-carbonic inclusions (Fig. 6H, J) always develop a vapor phase in the carbonic bubble, even if they are two-phase at room temperature. The melting temperature of CO_2 ($T_{m\,(CO_2)}$) ranges from –58.1° to –56.6°C with the majority of CO_2 melting occurring at –56.6°C (Fig. 7G). The carbonic phase always homogenized to the liquid ($T_{h\,(CO_2)}$) at temperatures ranging from 10.2° to 26.1°C with a mode around 24.0°C (Fig. 7H). Clathrate observed in these inclusions exhibits a typical Q2 melting behavior (Bakker and Brown, 2003). The clathrate melting temperatures ($T_{m(cl)}$) of primary inclusions range from 8.3° to 9.2°C, corresponding to salinities of 1.6 to 3.3 wt percent NaCl equiv (Diamond, 1992), with an average of 2.3 wt percent NaCl equiv (Fig. 7F), which is two to three times lower than the salinity of the type Ia aqueous inclusions. The $T_{m(cl)}$ of secondary inclusions range from 9.4° to 9.8°C, corresponding to salinities of 0.4 to 1.2 wt percent NaCl equiv (Fig. 7F). These inclusions commonly decrepitated at temperatures below 200°C, before total homogenization was attained. The 35 inclusions that did not decrepitate homogenized into the liquid phase at temperatures from 190° to 245°C, with a mode around 220°C (Fig. 7E). Raman spectroscopy of the carbonic phase in individual fluid inclusions showed that CO_2 is the dominant volatile (>96 mol %), N_2 is always detected (0.5–3.5 mol %), and CH_4 has been detected (up to 1.2 mol %) in a few inclusions (Table 2).

Type II aqueous-carbonic inclusions (Fig. 6K) also always develop a vapor phase in the carbonic bubble during cooling runs. Their $T_{m(CO_2)}$ ranged from –59.6° to –58.1°C (Fig. 7G). Homogenization of the CO_2 was always to the liquid phase between 6.3° to 20.9°C. The $T_{m(cl)}$ range from 9.5° to 10.7°C, corresponding to salinities of 0 to 8.9 wt percent NaCl equiv (Bakker and Brown, 2003). Total homogenization

FIG. 6. Microphotographs of fluid inclusions in quartz. A. Early milky quartz (thin section) from Shuiyindong. B. Primary and C. Secondary type Ia aqueous inclusions in the milky quartz from Shuiyindong. D. Photograph and sketch of early milky quartz from Yata. E. Primary and F. Secondary type Ia aqueous inclusions in the milky quartz from Yata. G. SEM-CL image of a main ore-stage quartz crystal, and H. Photographs of type Ib aqueous-carbonic inclusions from Yata. Circles denote the positions of inclusions analyzed by LA-ICP-MS. I. to L. Late drusy quartz crystal with types Ib, II, and III aqueous-carbonic and carbonic-rich inclusions from Yata, respectively. Note that two end-member fluid inclusion assemblages are cogenetic in (L). For the various fluid inclusion types refer to Table 1. Scale bar is 20 μm unless defined otherwise.

TABLE 1. Summary of Fluid Inclusion Types, Associated Mineral Assemblages, and Microthermometric Data

Deposit	Stage	Fluid inclusion assemblage	Microthermometric data						
		Generation	Type	Number	$T_{m\,(CO2)}$ (°C)	$T_{h(CO2)}$ (°C)	T_m (°C)	$T_{m(cl)}$ (°C)	T_h (°C)
Shuiyindong	Early-stage Vein quartz-pyrite	Primary in vein quartz crystals	Type Ia	14			–3.5 to –4.3		218 to 231
		Secondary in vein quartz crystals	Type Ia	18			–2.3 to –3.3		194 to 229
Yata	Early-stage Vein quartz-pyrite	Primary in vein quartz crystals	Type Ia	23			–3.0 to –4.1		190 to 258
	Main-stage Quartz-arsenian pyrite-arsenopyrite	Secondary in veinlet quartz crystals	Type Ia	22			–2.1 to –3.3		165 to 230 (190)
		Primary and secondary in veinlet quartz crystals	Type Ib	67	–58.1 to –56.6 (–56.6)	10.2 to 26.1 (24) L,		8.3 to 9.8 (9.5)	190 to 245 (220)
	Late-stage Quartz-stibnite-Realgar-orpiment	Secondary in veinlet quartz crystals	Type Ia	23			–1.2 to –4.5 (–3.5)		151 to 261 (190)
			Type II	6	–59.6 to–58.1	6.3 to 20.9 L,		9.5 to 10.7	205[1] to 232[1]
			Type III	25	–60.5 to –59.6 (–60.1)	–24.3 to –22.5 (–24.0) L,			

Notes: For microthermometric parameters, ranges (in parenthesis) and mode are given; $T_{m\,(CO2)}$ = final melting temperature of CO_2, $T_{h(CO2)}$ = homogenization temperature of CO_2, T_m = melting temperature of ice, $T_{m(cl)}$ = final melting temperature of clathrate, T_h = homogenization temperature; L = homogenize to liquid
[1] Decrepitation temperature

temperatures were not obtained because these inclusions decrepitated when heated to above 200°C. Raman spectroscopy revealed that their volatile phases contain major CO_2 (87–89 mol %), minor N_2 (10–14 mol %), and trace CH_4 (0.8 mol %; Table 2).

In the process of freezing (down to –180°C) and subsequent heating, type III carbonic inclusions (Fig. 6L) underwent the following sequence of phase transitions: S + V → L + V → L. The $T_{m(CO_2)}$ range from –60.5° to –59.6°C with the

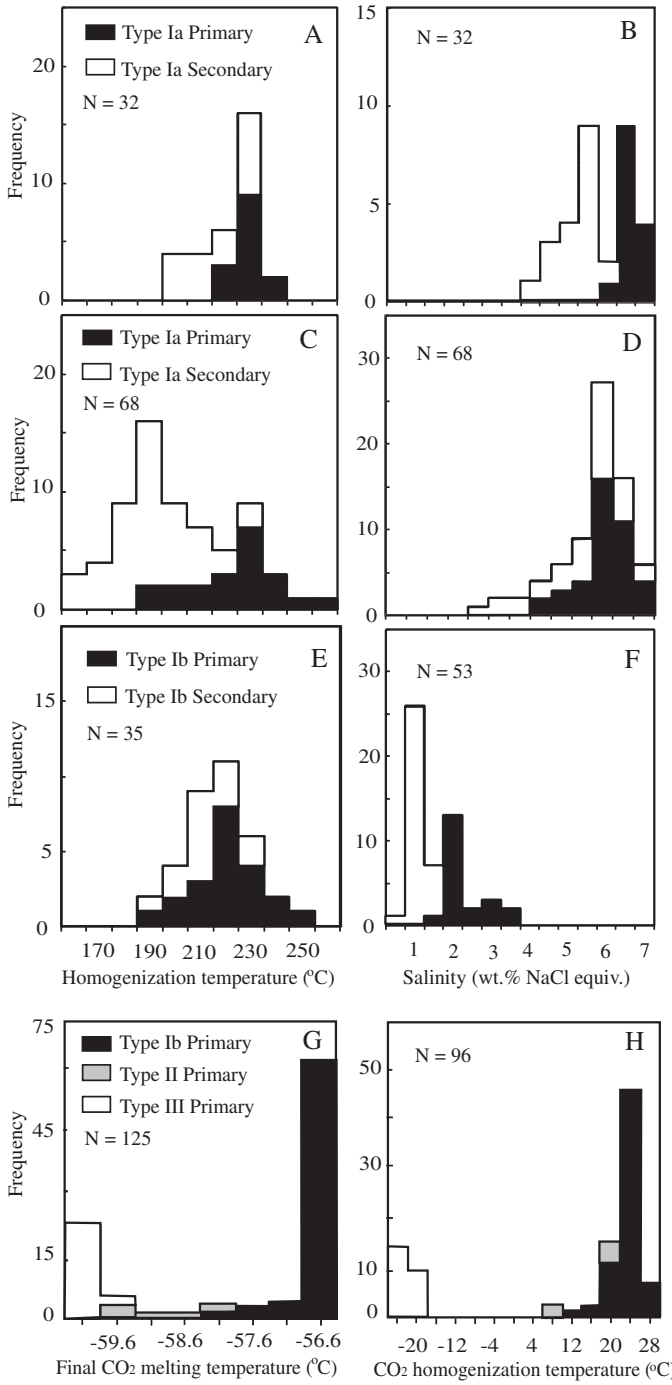

FIG. 7. Histogram of homogenization temperature, final CO_2 melting temperature, and salinity of fluid inclusions from Shuiyindong (A-B) and Yata (C-H).

TABLE 2. Chemical Compositions of Representive Aqueous–Carbonic and Carbonic–Rich Inclusions Obtained by Raman Spectroscopic Analysis and Corresponding Microthermometric Data from Yata

			Microthermometry						Raman data		
Stage	Quartz type	Inclusion	$T_{m(CO_2)}$ (°C)	$T_{h(CO_2)}$ (°C)	Mode	$T_{m(cl)}$ (°C)	T_h (°C)	Mode	CO_2	N_2	CH_4
Main-stage	Veinlet quartz crystals	41	–56.7	20.5	L	9.4	228	L	97.5	1.5	1.0
		42	–57.7	17.6	L	9.3	227	L	95.7	3.3	1.0
		55	–56.7	21.6	L	9.4	220	L	97.0	3.0	n.d.
		60	–56.8	22.2	L	8.8	215	L	96.8	2.0	1.2
		61	–56.6	22.9	L	9.4	210	L	99.5	0.5	n.d.
		65	–56.9	21.4	L		238	L	96.0	3.5	0.5
		66	–56.8	22.3	L		217	L	97.0	3.0	n.d.
		76	–56.7	23.4	L	9.6	223	L	96.8	2.5	0.7
		80	–56.7	23.3	L		206	L	98.2	1.8	n.d.
		93	–56.6	24.8	L	8.6	225	L	98.7	1.3	n.d.
		94	–56.7	24.5	L	9.4	210	L	97.5	1.8	0.7
		99	–56.7	17.9	L	9.0	247	L	96.5	2.7	0.8
		107	–56.7	20.8	L	9.8	216	L	97.2	1.9	0.9
Late stage	Veinlet quartz crystals	34	–58.7	6.3	L	9.5	232[1]		86.5	13.5	n.d.
		35	–58.6	7.8	L	9.3	228[1]		89.2	10.0	0.8
		11	–60.5	–24.3	L				71.0	27.2	1.8
		12	–60.3	–24.0	L				73.0	27.0	n.d.
		14	–60.2	–23.3	L				75.0	25.0	n.d.
		15	–60.2	–23.2	L				77.0	23.0	n.d.

Notes: n.d. = not detected, other abbreviations as in Table 1; Composition is given in mol percent
[1] Decrepitation temperatures

majority at –60.1°C (Fig. 7G). The $T_{h(CO_2)}$ of this type of inclusion range from –24.3° to –22.5°C (Fig. 7H) and were always into the liquid phase. Total homogenization temperatures could not be measured reliably owing to optical limitations (Diamond, 2003). Raman spectroscopy showed that the volatile phase of type III inclusions contains major CO_2 (71–77 mol %), minor N_2 (23–27 mol %), and trace CH_4 (up to 1.8 mol %; Table 2).

Bulk compositions of aqueous-carbonic and carbonic-rich fluids

Aqueous-carbonic inclusions in the main stage of pyrite-arsenopyrite-quartz veins and late stage of stibnite-realgar-orpiment-quartz veins at Yata have 10 to 15 vol percent volatile phase (nearly pure CO_2), regardless of the sample localities. Calculated density of the volatile phase varies from 0.72 to 0.82 g/cm^3, with an average of 0.75 g/cm^3. Calculated bulk compositions showed that the fluids are dominated by H_2O (91–92 mol %) and CO_2 (6.3–8.4 mol %, with an average of 7.6 mol %). Their bulk densities range from 0.97 to 0.99 g/cm^3. Their average salinities vary from 0.9 to 2.3 wt percent NaCl equiv.

Calculated bulk compositions of carbonic-rich inclusions in the late stage of stibnite-realgar-orpiment-quartz veins at Yata are dominantly CO_2 (58–64 mol %), N_2 (19.2–23.7 mol %), and H_2O (12.5–22.8 mol %), and trace CH_4 (up to 1.6 mol %), with volatile phase densities and bulk densities of 0.75 to 0.80 and 0.77 to 0.82 g/cm^3, respectively.

Pressure and Temperature Estimation

The compositions of type Ib inclusions plot close to the solvus of the H_2O-CO_2 system at 1.0 kb in Figure 8A. It is possible that the fluids of these inclusions may represent one end member produced by unmixing of H_2O-CO_2 fluids. The compositions of a few type II inclusions plot in the two-phase field in Figure 8A. These inclusions may represent mechanical mixtures of two immiscible fluid phases. The local occurrence of type II inclusions at Yata indicates that the hydrothermal fluid reached a state of immiscibility at some time in its history (Diamond, 1990). Type III inclusions plot close to the 1.0 kb solvus in Figure 8A. If they coexisted with type Ib inclusions, then these inclusions may represent another end member produced by unmixing of H_2O-CO_2 fluids.

The minimum P-T conditions of inclusion entrapment are constrained by intersecting points using the range of homogenization temperatures of type Ib inclusions (190°–245°C) and the minimum of the bubble curves of 6 mol percent CO_2 (Fig. 8B). The defined area in Figure 8B (shaded) ranges from 450 to 1,150 bars, corresponding to a depth of 1.7 to 4.3 km under lithostatic load, using the average density of sedimentary rocks in southwestern Guizhou (2.67 g/cm^3: Wang et al., 1995) and 4.5 to 11.5 km assuming hydrostatic pressure. As Yata was controlled by a fault, the estimated pressure may have been fluctuating between hydrostatic and lithostatic pressures. Decompression associated with episodes of faulting may have caused the immiscibility in the late stage of stibnite-realgar observed in this deposit. Zhang et al. (2003) previously estimated pressures for the Lannigou deposit ranging from 600 to 1,700 bars based on the CO_2-bearing fluid inclusions, corresponding to a depth of 2.2 to 6.3 km under lithostatic conditions or an unlikely 6 to 17 km under hydrostatic load. CO_2 contents of fluid inclusions at Yata (6–8 mol %) are somewhat lower than those of many orogenic lode gold deposits (10–25 mol % CO_2: Ridley and Diamond, 2000) but higher than those of Carlin-type gold deposits in Nevada (2–4 mol % CO_2: Hofstra and Cline, 2000). It is, therefore, reasonable to infer that the Yata deposit may have formed at depths intermediate between orogenic-type gold deposits and those of the Carlin trend in Nevada.

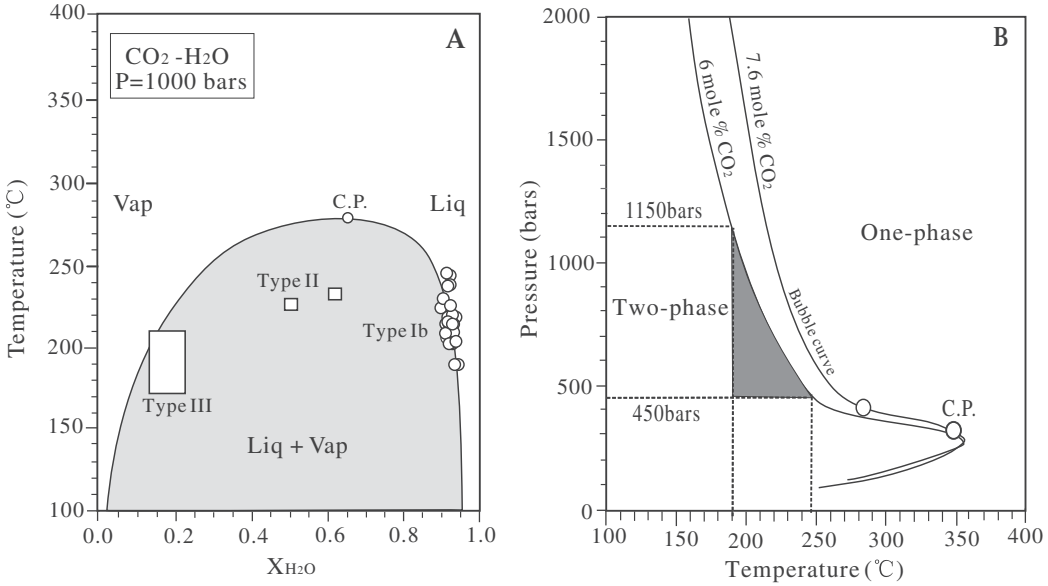

FIG. 8. A. T-X diagram of the H_2O-CO_2 system at 1.0 kbar based on experimental data from Tödheide and Franck (1963) and Takenouchi and Kennedy (1964). B. P-T diagram showing the range of possible P-T conditions during mineralization at Yata. The miscibility boundaries for fluids with 6 and 7.6 mol percent CO_2 are from experimental data of the H_2O-CO_2 system of Tödheide and Franck (1963) and Takenouchi and Kennedy (1964).

LA-ICP-MS Microanalyses of Fluid Inclusions

Representative fluid inclusion types from both deposits were analyzed by LA-ICP-MS. Boron, Na, Mg, K, Mn, Fe, Cu, Pb, Zn, As, Sb, Au, Ag, Sr, Cs, and U concentrations were recorded in all analyses. Fluid inclusions of all types consistently contain detectable quantities of B, Na, K, Sr, Cs, As, and Sb, whereas Mg, Mn, Fe, Ag, Cu, Pb, Zn, U, and Au are commonly near or below the limit of detection (LOD). Gold was above the 1σ limit of detection in five aqueous inclusions and in 12 aqueous-carbonic inclusions. The element concentrations in each inclusion are listed in the Appendix. The average element concentrations in the different fluid inclusion types are given in Table 3.

The results show systematic variations in metal concentrations of fluids between the different fluid inclusion types

TABLE 3. Summary of Fluid Inclusion Composition (in μg/g) Analyzed by Laser Ablation ICP-MS

	Shuiyindong		Yata				
	Early-stage (Qz-py)		Early-stage (Qz-py)	Main-stage (Qz-As-py-Asp)	Late-stage (Qz-cal-real-stb)		
Element	SYD035-Q2	SYD035-Q1	Q64	YT-5	YT1-010	YT1-012	YT1-013
B	1100 (100)[1]	800 (200)	700 (400)	300 (100)	100 (40)	200 (100)	100 (50)
Na	26400 (400)	20500 (200)	21600 (100)	7700 (190)	3200 (80)	3700 (900)	2400 (40)
K	780 (120)	400 (240)	500 (260)	400 (500)	280 (250)	100 (1000)	100[2]
Sr	230 (30)	140 (40)	40 (10)	4 (8)	10 (10)	6 (4)	1[2]
Cs	16 (8)	10 (4)	9 (6)	5 (3)	6 (7)	6 (10)	2 (1)
As	80 (30)	90 (20)	200 (120)	100 (50)	200 (200)	250 (160)	70 (50)
Sb	20[2]	10 (4)	20[2]	10 (6)	10 (6)	90 (60)	10 (4)
Au	3.8 (0.5)	b.d.	5.7 (2.3)	0.4 (0.2)	b.d.	b.d.	b.d.
Ag	20[2]	10[3]	20[3]	b.d.	b.d.	10[3]	b.d.
Fe	b.d.	b.d.	b.d.	b.d.	b.d.	b.d.	b.d.
Cu	50[2]	80[3]	80[3]	b.d.	b.d.	200[2]	b.d.
Pb	5[2]	b.d.	30[3]	b.d.	8[2]	25[3]	b.d.
Zn	b.d.	b.d.	200[2]	b.d.	b.d.	b.d.	b.d.
Mg	60[2]	200[3]	b.d.	80[3]	b.d.	b.d.	b.d.
U	1[3]	b.d.	6[3]	b.d.	1[3]	5[3]	b.d.

Notes: b.d. = below detection; abbreviations: Asp = arsenopyrite, As-py = arsenian pyrite, cal = calcite, py = pyrite, Qz = quartz, real = realgar, stb = stibnite

[1] Numbers in parenthesis are 1σ for an inclusion assemblage of which several inclusions have been analyzed individually

[2] Numbers based on a single inclusion analysis with concentrations above the detection limit

[3] Numbers based on the average of multiple inclusion analyses with concentrations above the detection limit (3δ)

(Table 3, Fig. 9). The B, Na, K, Cs, Sr, As, Sb, and Au concentrations are higher in aqueous inclusions (type Ia). Secondary aqueous inclusions have lower concentrations of these elements than primary aqueous inclusions. Concentrations of these elements are progressively lower in the aqueous-carbonic inclusions, but they do not decrease at the same rate. The Sr decrease is steeper than that of the other alkali metals (Fig. 9), indicating that selective precipitation of Sr-bearing minerals occurred during mineralization. Gold concentrations in the aqueous inclusions from Shuiyindong and Yata range from 3.8 ± 0.5 to 5.7 ± 2.3 μg/g (Table 3), whereas the aqueous-carbonic inclusions from Yata have lower concentrations of Au, ranging from 0.1 to 0.8 μg/g (App., sample YT-5). Arsenic concentrations are approximately constant in the aqueous inclusions at Shuiyingdong, but decrease from 200 ± 120 μg/g in the aqueous inclusions to 100 ± 50 μg/g in the aqueous-carbonic inclusions at Yata. Antimony concentrations in aqueous-carbonic inclusions in the late stibnite-realgar-quartz veins at Yata are higher (up to 90 μg/g) than in the other inclusions. A decrease in Sb and As concentrations is probably due to precipitation of stibnite and realgar, which have been observed within late-stage quartz growth zones.

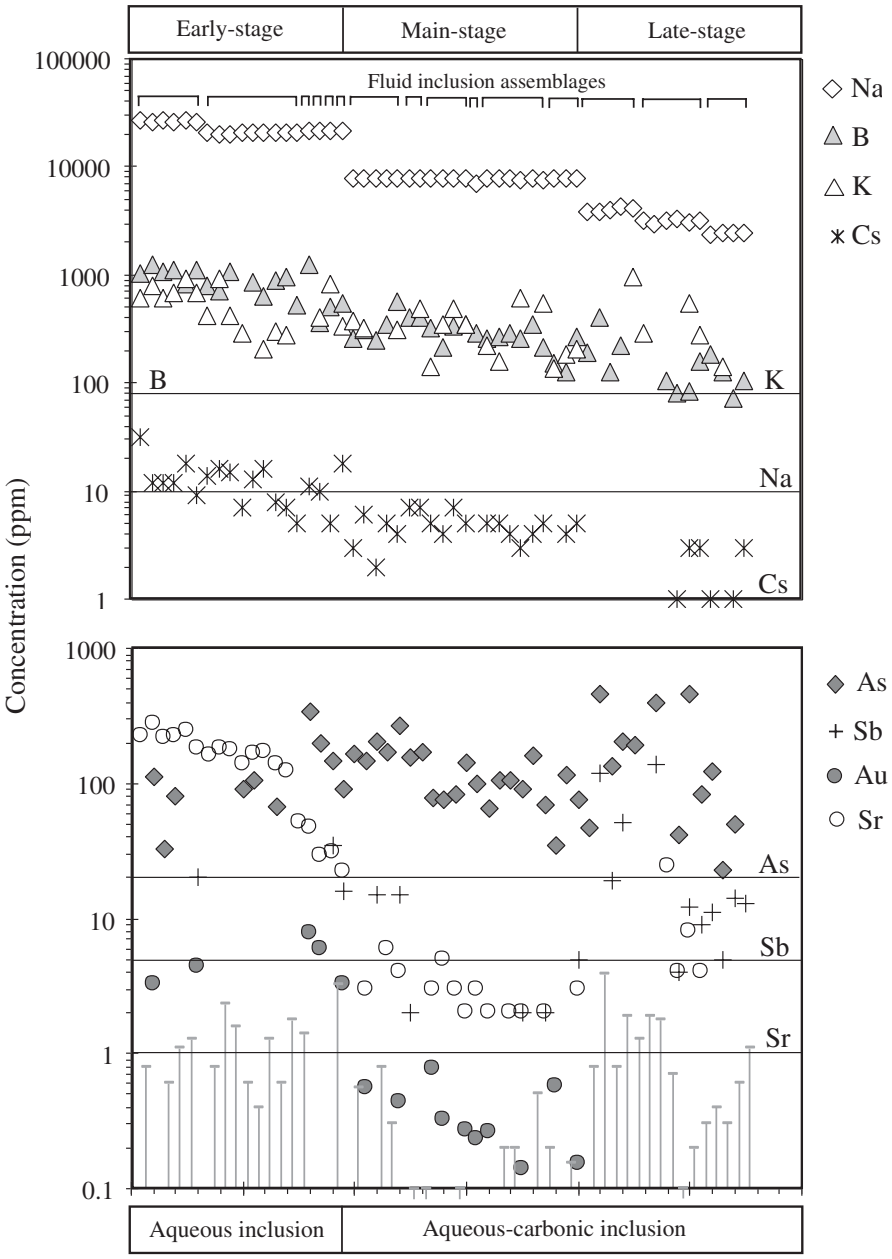

FIG. 9. Chemical evolution of fluid inclusion assemblages across the paragenetic sequences based on LA-ICP-MS analysis. The relative timing of fluid inclusion assemblages is based on crosscutting relationships and quartz growth zones revealed by cathodoluminescence. Note the general decrease in element concentrations, except for As and to a lesser extent Sb, across the ore depositional event. The parallel and vertical gray lines represent the limit of detection of B, Na, K, Cs, As, Sb, Sr at 3σ and Au at 1σ, respectively.

However, other cations, such as Mg, are generally below the limit of detection in the fluid inclusions. Iron, which has a typical detection limit of 400 μg/g in LA-ICP-MS analysis, was not detected in any fluid inclusions analyzed during this study.

Discussion

Interpretation of fluid inclusion paragenesis and LA-ICP-MS data

LA-ICP-MS results showed that aqueous inclusions in barren milky quartz veins from both deposits have high concentrations of the characteristic ore elements (As, Sb, and Au) compared to aqueous-carbonic inclusions. This fluid is interpreted to approximate the mineralizing fluid, which was responsible for precipitation of early milky quartz veins. Aqueous-carbonic fluid is interpreted to correspond to the main-stage gold-bearing fluid. The higher CO_2 content of this fluid is interpreted to result from carbonate dissolution at the level of the deposits. The decrease of Au and As in aqueous-carbonic inclusions is interpreted to be due to deposition of disseminated gold-bearing arsenian pyrite and arsenopyrite in the main mineralization stage. Covariance of Au and As, as well as Sb and Sr, in ore fluids (Figs. 9, 10A), as observed in EMPA analyses of gold-bearing arsenian pyrite and bulk ore samples (Fig. 10B, C), is interpreted to reflect precipitation of As and Sb sulfides and gold concurrently with Sr-bearing carbonate. This is consistent with petrographic observations that gold-bearing arsenian pyrite and arsenopyrite are accompanied in the main mineralization stage by the Fe-poor

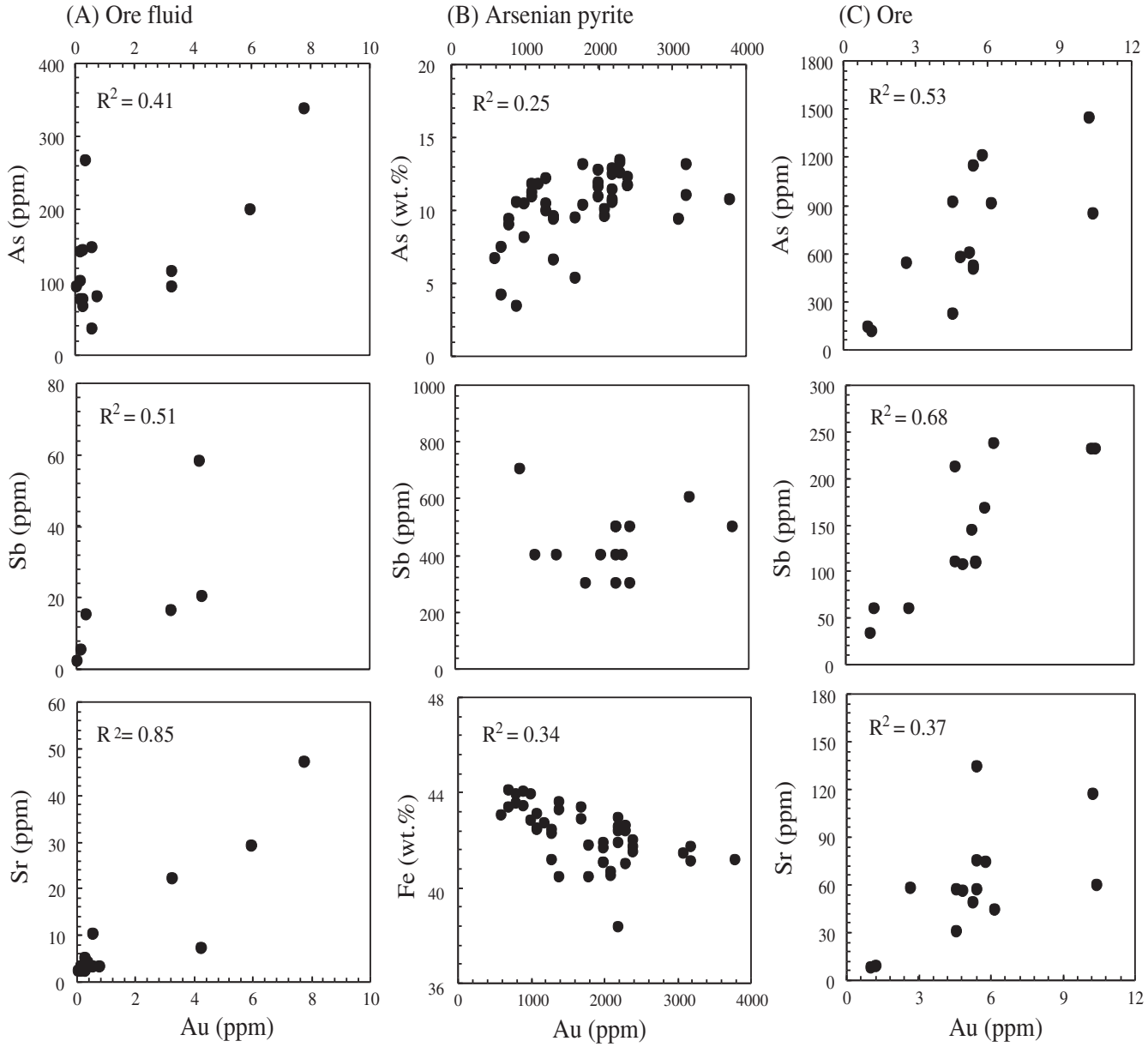

FIG. 10. Correlation of Au and As, Sb, Sr in ore fluid (A), gold-bearing arsenian pyrite (B), and ore (C). The EMPA data of arsenian pyrite and bulk ore samples are from Su et al. (2008) and Xia (2005), respectively.

hydrothermal dolomite or calcite in both deposits (Fig. 3C, I). Dilution also may have occurred during gold mineralization because the salinities of the inclusions decrease two to three fold from aqueous inclusions to aqueous-carbonic inclusions.

Source of fluids

Oxygen and hydrogen isotope compositions of early barren milky quartz veins and clay minerals (<2 μm) in the mineralized rock from Shuiyindong have been reported by Hofstra et al. (2005). The milky quartz veins have a narrow range of high $\delta^{18}O$ values (21–27‰). Calculated $\delta^{18}O_{(H_2O)}$ values for fluids in these samples vary from 10.5 to 16.5 per mil, using a homogenization temperature of 230°C from this study and the quartz-water isotopic equilibrium fractionation equation of Friedman and O'Neil (1977). Calculated $\delta^{18}O_{(H_2O)}$ and $\delta D_{(H_2O)}$ values for fluids in equilibrium with clay minerals in the mineralized rocks at Shuiyindong range from 4 to 10 and –56 to –68 per mil, respectively (Hofstra et al., 2005). Similar fluid calculations for clay minerals in the mineralized rocks from the Zimudang deposit, located 15 km west of Shuiyindong on the same large-scale dome structure, indicate $\delta^{18}O_{(H_2O)}$ and $\delta D_{(H_2O)}$ values from 13 to 16 and –35 to –40 per mil, respectively (Hofstra et al., 2005).

Li et al. (1989) and Zhu et al. (unpub. data) reported oxygen for the main ore quartz and the late ore calcite from Yata. The main ore quartz has a narrow range of $\delta^{18}O$ values (20.9–26.1‰), similar to milky quartz veins at Shuiyindong. The calculated $\delta^{18}O_{(H_2O)}$ values for the main ore fluids from Yata vary from 9.9 to 15.1 per mil at 220°C. The $\delta^{18}O_{(H_2O)}$ values of late ore fluids (8.1–10.9‰) were calculated from measured $\delta^{18}O$ calcite values (18.2–20.8‰), the minimum homogenization temperature of 190°C for CO_2-bearing fluid inclusions within calcite (Zhang et al., 2003) and the calcite-water isotopic equilibrium fractionation equation of Friedman and O'Neil (1977). The $\delta D_{(H_2O)}$ values of water extracted from inclusion fluids in the main ore quartz at Yata range from –51.1 to –78.8 per mil (Li et al., 1989), significantly higher than the average $\delta D_{(H_2O)}$ value of local meteoric water during the Jurassic and Cretaceous (–85‰: Han et al., 1999).

The $\delta^{18}O_{(H_2O)}$ and $\delta D_{(H_2O)}$ values plot within or close to the metamorphic-water box (Hofstra et al., 2005, fig. 3), suggesting that the ore fluids are characterized by a predominantly metamorphic component. There is no evidence for meteoric water involvement, but a deep magmatic component cannot be excluded.

Processes of gold deposition

Recent studies of Carlin-type deposits in Nevada have concluded that gold-rich arsenian pyrite precipitated from H_2S-rich fluids, which sulfidized iron-bearing minerals in the host rocks (Hofstra et al., 1991; Hofstra and Cline, 2000; Kesler et al., 2003). The chemical reaction of cooling H_2S-rich fluids in contact with iron-poor carbonate-bearing sedimentary rocks has been calculated from thermodynamic data by Heinrich (2005). An important prediction is that Au solubility may remain high to temperatures as low as 150°C, provided that an excess of H_2S over Fe is maintained in a moderately oxidized hydrothermal fluid, the pH of which is kept close to neutral by carbonate dissolution (Heinrich, 2005, fig. 6). This fluid-chemical evolution path can equally apply to fluids of magmatic or metamorphic origin but clearly matches the low Fe contents of fluids measured in the inclusions from the Shuiyindong and Yata deposits.

At the strata-bound Shuiyindong deposit, there is no evidence for significant phase separation during the main mineralization stage. At the fault-controlled Yata deposit, phase separation was minor during gold mineralization and common in the late stibnite-realgar stage. This fluid inclusion evidence suggests that phase separation was not the key process for deposition of gold and arsenian pyrite. The low Fe contents in the ore fluids (below 400 μg/g) measured by LA-ICP-MS of fluid inclusions and many relict inclusions of ferroan carbonate (with up to 7.0 wt % Fe determined by EMPA: Su et al., 2008) enclosed in the jasperoidal quartz crystals suggest that iron in sulfide minerals was probably derived from dissolution of ferroan carbonate in the host rocks, as has been documented in Carlin-type gold deposits in Nevada by lithogeochemistry of ores (Hofstra et al., 1991; Hofstra and Cline, 2002). Sulfidation of ferroan carbonate-rich host rocks by H_2S-rich ore fluids containing $Au(HS)_2^-$ or $Au(HS)^0$ (Seward, 1973, 1991), along with arsenic as $H_3AsO_{3(aq)}$ complex (Heinrich and Eadington, 1986; Pokrovski et al., 2002), would have effectively extracted gold from solution and transformed primary ferroan carbonate to secondary gold-bearing arsenian pyrite, possibly by a coupled reaction such as the following:

$$2FeCO_3 + 2H_3AsO_{3\,(aq)} + H_2S_{(aq)} + 2Au(HS)_{2(aq)}^- + H_{2\,(g)} = Fe(S, As)_2 \cdot Au_2S^0 + FeS_2 + CO_{3(aq)}^{-2} + CO_{2\,(g)} + 7H_2O.$$

Any loss of CO_2 by fluid phase separation would further promote the formation of gold-bearing arsenian pyrite by such a reaction. This is consistent with petrographic observations that gold-bearing arsenian pyrite and arsenopyrite occur together with Fe-poor hydrothermal dolomite (Fig. 3C). Moreover, it can explain the covariance of Au, As, Sb, and Sr contents of the ore fluids (Fig. 9). The reaction involves reduction of As (+III) and Au (+I) by consumption of $H_{2\,(g)}$, which can be provided by reaction of the metal-transporting fluids with the local organic-rich sediments. This situation is likely to occur where fluids are channeled into a fluid conduit (e.g., along the unconformity between the Maokou Limestone and the Longtan Formation at Shuiyindong or the reverse faults at Yata). Here, they reacted with carbonaceous and Fe carbonate-rich host rock, or were mixed with Fe^{+2}- and CH_4-bearing pore fluids previously equilibrated with the reduced host-rock package, to deposit arsenian pyrite and arsenopyrite that host most of the gold in the deposits. The generation of secondary pervasive permeability and porosity by carbonate dissolution from the host rocks favors fluid focusing and the formation of strata-bound orebodies (Heinrich, 2005), as is the case in the Shuiyindong. Therefore, fluid reduction and sulfidation of wall-rock iron by H_2S-rich ore fluids are proposed to be the most important mechanism of gold deposition as auriferous arsenian pyrite in the Chinese Carlin-type gold deposits.

Genetic models previously proposed for Carlin-type deposits in Nevada fall into three groups involving magmatic (Radtke et al., 1980; Ressel et al., 2000), metamorphic (Groves et al., 1998; Cline and Hofstra, 2000), and deeply or shallowly circulated meteoric waters (Ilchik and Barton, 1997; Emsbo

et al., 2003). Our study of Carlin-type deposits in Guizhou indicates that the ore fluids are of low salinity but rich in high-density CO_2, and stable isotope data are consistent with a dominant metamorphic fluid source. The ore-forming fluids have extremely high contents of the characteristic ore elements (As, Sb, and Au), and the mineralogical characteristics and high gold grade of the deposits can be explained by interaction of such fluids with chemically reactive carbonate-, iron-, and carbon-rich sedimentary host rocks. The deposits formed at similar temperatures as epithermal gold deposits, but at significantly higher pressure and greater depths (4–6 km), consistent with regional-metamorphic temperature gradients. Their thermal regime and ore fluid characteristics are similar to those of the broad group of orogenic gold deposits, raising the possibility that the Carlin-type deposits in Guizhou might be the basin-hosted and relatively cool end member of the crustal continuum of orogenic gold deposit formed from fluids liberated by deep metamorphic dehydration or magmatism (Groves, 1993; Groves et al., 1998; Pettke et al., 2000).

Acknowledgments

We are grateful to Guizhou Zijin Gold Mines for access to samples and to Jianzhong Liu and Chuanqin Liu for geologic guidance and discussion during fieldwork. We would like to thank Claudia Pudack and Leonhard Klemm for their help with microthermometric measurement and Kalin Kouzmanov for his help with SEM-CL imaging. Review comments by Albert H. Hofstra improved presentation and scientific arguments. Editor Mark Hannington, David Cooke, Ross Large, and an anonymous referee are thanked for their thoughtful and thorough reviews. This work was supported by the National Science Foundation of China (Grants 40672067, 49873029), Key State Basic Research Program of China (Grant 2007CB411402), and China Postdoctoral Science Foundation (Grant 20060390740) to complete part of the analytical work at ETH Zürich, Switzerland. The State Key Laboratory for Mineral Deposits Research, Nanjing University, China, provided financial support for laser Raman spectroscopy analysis.

November 27, 2007; January 12, 2009

REFERENCES

Arehart, G.B., 1996, Characteristics and origin of sediment-hosted gold deposits: A review: Ore Geology Reviews, v. 11, p. 383–403.

Ashley, R.P., Cunningham, C.G., Bostick, N.H., Dean, W.E., and Chou, I.M., 1991, Geology and geochemistry of three sedimentary-rock-hosted disseminated gold deposits in Guizhou Province, People's Republic of China: Ore Geology Reviews, v. 6, p. 133–151.

Bakker, R.J., 1997, Clathrates: Computer programs to calculate fluid inclusion V-X properties using clathrate melting temperatures: Computers and Geosciences, v. 23, p. 1–18.

——1999, Adaptation of the Bowers and Helgeson (1983) equation of state to the H_2O-CO_2-CH_4-N_2-NaCl system: Chemical Geology, v. 154, p. 225–236.

Bakker, R.J., and Brown, P.E., 2003, Computer modelling in fluid inclusion research: Mineralogical Association of Canada Short Course Series, v. 32, p. 175–212.

Bodnar, R.J., 1993, Revised equation and table for determining the freezing point depression of H_2O-NaCl solutions: Geochimica et Cosmochimica Acta, v. 57, p. 683–684.

Bodnar, R.J., Reynolds, T.J., and Kuehn, C.A., 1985, Fluid inclusion systematics in epithermal systems: Reviews in Economic Geology, v. 2, p. 73–79.

Bowers, T.S., and Helgeson, H.C., 1983, Calculation of the thermodynamic and geochemical consequences of nonideal mixing in the H_2O-CO_2-NaCl on phase relations in geological systems: Equation of state for H_2O-CO_2-NaCl fluids at high pressures and temperatures: Geochimica et Cosmochimica Acta, v. 47, p. 1247–1275.

Burke, E.A.J., 2001, Raman microspectrometry of fluid inclusions: Lithos, v. 55, p. 139–158.

Cline, J.S., and Hofstra, A.H., 2000, Ore-fluid evolution at the Getchell Carlin-type gold deposit, Nevada, USA: European Journal of Mineralogy, v. 12, p. 195–212.

Cunningham, C.G., Ashely, R.P., Chou, I.M., Huang, Z., Wan, C., and Li, W., 1988, Newly discovered sedimentary rock-hosted disseminated gold deposits in the People's Republic of China: Economic Geology, v. 83, p. 1462–1467.

Diamond, L.W., 1990, Fluid inclusion evidence for P-V-T-X evolution of hydrothermal solutions in late-alpine gold-quartz veins at Brusson, Val D'Ayas, northwest Italian Alps: American Journal of Science, v. 290, p. 912–958.

——1992, Stability of CO_2 clathrate + CO_2 liquid + CO_2 vapour + aqueous KCl-NaCl solutions: Experimental determination and application to salinity estimates of fluid inclusions: Geochimica et Cosmochimica Acta, v. 56, p. 273–280.

——2001, Review of the systematics of CO_2-H_2O fluid inclusions: Lithos, v. 55, p. 69–99.

——2003, Introduction to gas-bearing aqueous fluid inclusions: Mineralogical. Association of Canada Short Course Series, v. 32, p. 101–158.

Duan, Z., Møller, N., and Weare, J.H., 1992, Molecular dynamics simulation of PVT properties of geological fluids and a general equation of state of nonpolar and weakly polar gases up to 2000K and 20,000 bar: Geochimica et Cosmochimica Acta, v. 56, p. 3839–3845.

——1996, A general equation of state for supercritical fluid mixtures and molecular dynamics simulation of mixture PVTX properties: Geochimica et Cosmochimica Acta, v. 60, p. 1209–1216.

Emsbo, P., Hofstra, A.H., Lauha, E.A., Griffin, G.L., and Hutchinson, R.W. 2003, Origin of high-grade gold ore, source of ore fluid components, and genesis of the Meikle and neighboring Carlin-type deposits, northern Carlin trend, Nevada: Economic Geology, v. 98, p. 1069–1105.

Friedman, I., and O'Neil, J.R., 1977, Compilation of stable isotope fractionation factors of geochemical interest: U.S. Geological Survey Professional Paper 440-KK, p. 1–12.

Groves, D.I., 1993, The crustal continuum model for late-Archaean lode-gold deposits of the Yilgarn Block, Western Australia: Mineralium Deposita, v. 28, p. 366–374.

Groves, D.I., Goldfarb, R.J., Gebre-Mariam, M., Hagemann, S.G., and Robert, F., 1998, Orogenic gold deposits: A proposed classification in the context of their crustal distribution and relationships to other gold deposit types: Ore Geology Reviews, v. 13, p. 7–27.

Günther, D., and Heinrich, C.A., 1999, Enhanced sensitivity in laser ablation ICP-mass spectrometry using helium-argon mixtures as aerosol carrier: Journal of Analytical Atomic Spectrometry, v. 14 p. 1363–1368.

Günther, D., Audétat, A., Frischknecht, R., and Heinrich, C.A., 1998, Quantitative analysis of major, minor, and trace elements in fluid inclusions using laser ablation-inductively coupled plasma mass spectrometry: Journal of Analytical Atomic Spectrometry, v. 13, p. 263–270.

Hall, D.L., Sterner, S.M., and Bodnar, R.J., 1988, Freezing point depression of NaCl-KCl-H_2O solutions: Economic Geology, v. 83, p. 197–202.

Han, Z.J., Wang, Y.G., Feng, J.Z., Chen, T.J., Luo, X.H., and Liu, Y.H., 1999, The geology and exploration of gold deposits in southwestern Guizhou: China, Guizhou Science and Technology Press, p. 1–146 (in Chinese with English abs.).

Heinrich, C.A., 2005, The physical and chemical evolution of low-salinity magmatic fluids at the porphyry to epithermal transition: A thermodynamic study: Mineralium Deposita, v. 39, p. 864–889.

Heinrich, C.A., and Eadington, P.J., 1986, Thermodynamic predictions of the hydrothermal chemistry of arsenic, cassiterite-arsenopyrite-base metal sulfide deposits: Economic Geology, v. 81, p. 511–529.

Heinrich, C.A., Pettke, T., Halter, W.E., Aiger-Torres, M., Audétat, A., Günther, D., Hattendorf, B., Bleiner, D., Guillong, M., and Horn, I., 2003, Quantitative multi-element analysis of minerals, fluid and melt inclusions by laser-ablation inductively-coupled-plasma mass-spectrometry: Geochimica et Cosmochimica Acta, v. 67, p. 3473–3496.

Hofstra, A.H., and Cline, J.S., 2000, Characteristics and models for Carlin-type gold deposits: Reviews in Economic Geology, v. 13, p. 163–220.

Hofstra, A.H., Leventhal, J.S., Northrop, H.R., Landis, G..P., Rye, R.O., Birak, D.J., and Dahl, A.R., 1991, Genesis of sediment-hosted disseminated gold deposits by fluid mixing and sulfidization: Chemical-reaction-path modeling of ore-depositional processes documented in the Jerritt Canyon district, Nevada: Geology, v. 19, p. 36–40.

Hofstra, A.H., Zhang, X.C., Emsbo, P., Hu, R.Z., Su, W.C., Christiansen, W.D., Fu, S.W., and Theodorakos, P., 2005, Source of ore fluids in Carlin-type gold deposits in the Dian-Qian-Gui area and West Qinling belt, P.R. China: Implications for genetic models, *in* Mao, J.W., and Bierlein, F.P., eds., Mineral deposits research: Meeting the global challenge: Heidelberg, Springer-Verlag, v. 1, p. 533–536.

Hu, R.Z., Su, W.C., Bi, X.W., Tu, G.Z., and Hofstra, A.H., 2002, Geology and geochemistry of Carlin-type gold deposits in China: Mineralium Deposita, v. 37, p. 378–392.

Ilchik, R.P., and Barton, M.D., 1997, An amagmatic origin of Carlin deposits: Economic Geology, v. 92, p. 269–288.

Kesler, S.E., Fortuna, J., Ye, Z.J., Alt, J.C., Zohar, D.P., Borhauer, J., and Chryssoulis, S.L., 2003, Evaluation of the role of sulfidation in deposition of gold, Screamer section of the Betze-Post Carlin-type deposit, Nevada: Economic Geology, v. 98, p. 1137–1157.

Li, W.K., Jiang, X.S., Ju, R.H., Meng, F.Y., and Zhang, S.X., 1989, The geological characteristics and metallogenesis of disseminated gold deposits in southwestern Guizhou, China, *in* Regional ore-forming condition of main gold deposit styles in China, southwestern Guizhou: Beijing, China, Geological Publishing House, v. 6, p. 1–86 (in Chinese).

Li, Z.X., and Li, X.H., 2007, Formation of the 1300-km-wide intracontinental orogen and postorogenic magmatic province in Mesozoic South China: A flat-slab subduction model: Geology, v. 35, p. 179–182.

Liu, J.M., Ye, J., Ying, H.L., Liu, J.J., Zheng, M.H., and Gu, X.X., 2002, Sediment-hosted micro-disseminated gold mineralization constrained by basin paleo-topograhic highs in the Youjiang basin, South China: Journal of Asian Earth Sciences, v. 20, p. 517–533.

Liu, J.Z., 2001, Geological characteristics of Yanshang Carlin-type gold deposit: Guizhou Geology, v. 18, p. 174–178 (in Chinese with English abs.).

——2003, Ore characteristics and gold occurrence of the Shuiyindong gold deposit, Guizhou: Guizhou Geology, v. 20, p. 30–34 (in Chinese with English abs.).

Mao, S.H., 1991, Occurrence and distribution of invisible gold in a Carlin-type gold deposit in China: American Mineralogist, v. 76, p. 1964–1972.

Murowchick, J.B., 1992, Marcasite inversion and the petrographic determination of pyrite and ancestry: Economic Geology, v. 87, p. 1141–1152.

Peters, S.G., Huang, J., Li, Z., and Jing, C., 2007, Sedimentary rock-hosted Au deposits of the Dian-Qian-Gui area, Guizhou, and Yunnan provinces, and Guangxi district, China: Ore Geology Reviews, v. 31, p. 170–204.

Pettke, T., Diamond, L.W., and Kramers, J.D., 2000, Mesothermal gold lodes in the north-western Alps: A review of genetic constraints from radiogenic isotopes: European Journal of Mineralogy, v. 12, p. 213–230.

Pettke, T., Halter, W.E., Webster, J.D., Aigner-Torres, M., and Heinrich, C.A., 2004, Accurate quantification of melt inclusion chemistry by LA-ICPMS: A comparison with EMP and SIMS and advantages and possible limitations of these methods: Lithos, v. 78, p. 333–361.

Pokrovski, G.S., Kara, S., and Roux, J., 2002, Stability and solubility of arsenopyrite, FeAsS, in crustal fluids: Geochimica et Cosmochimica Acta, v. 66, p. 2361–2378.

Radtke, A.S., Rye, R.O., and Dickson, F.W., 1980, Geology and stable isotope studies of the Carlin gold deposit, Nevada: Economic Geology, v. 75, p. 641–672.

Ressel, M.W., Noble, D.C., Henry, C.D., and Trundel, W.S., 2000, Dike-hosted ores of the Beast deposit and importance of Eocene magmatism in gold mineralization of Carlin trend: Economic Geology, v. 95, p. 1417–1444.

Ridley, J.R., and Diamond, L.W., 2000, Fluid chemistry of orogenic lode gold deposits and implications for genetic models: Reviews in Economic Geology, v. 13, p. 141–162.

Roedder, E., 1984, Fluid inclusions: Reviews in Mineralogy, v. 12, 644 p.

Seward, T.M., 1973, Thio-complexes of gold in hydrothermal ore solutions: Geochimica et Cosmochimica Acta, v. 37, p. 379–399.

——1991, The hydrothermal geochemistry of gold, *in* Foster, R.P., eds., Gold metallogeny and exploration: Glasgow, Blackie, p. 37–62.

Sterner, S.M., and Bodnar, R.J., 1984, Synthetic fluid inclusions in natural quartz: 1. Compositional types synthesized and applications to experimental geochemistry: Geochimica et Cosmochimica Acta, v. 48, p. 2659–2668.

Sterner, S.M., Hall, D.L., and Bodnar, R.J., 1988, Synthetic fluid inclusions, V. Solubility relations in the system NaCl-KCl-H_2O under vapor-saturated conditions: Geochimica et Cosmochimica Acta, v. 52, p. 989–1005.

Su, W.C., 2002, The hydrothermal fluid geochemistry of the Carlin-type gold deposits in southwestern Yangtze craton, China: Unpublished Ph.D. thesis, Guiyang, China, Institute of Geochemistry, Chinese Academy of Sciences (in Chinese with English abs.).

Su, W.C., Xia, B., Zhang, H.T., Zhang, X.C., and Hu, R.Z., 2008, Visible gold in arsenian pyrite at the Shuiyindong Carlin-type gold deposit, Guizhou, China: Implications for the environment and processes of ore formation: Ore Geology Reviews, v. 33, p. 667–679.

Su, W.C., Hu, R.Z., Xia, B., Xia, Y. and Liu, Y.P., 2009, Calcite Sm-Nd isochron age of the Shuiyindong Carlin-type gold deposit, Guizhou, China: Chemical Geology, v. 258, p. 269–274.

Suo, S.T., Bi, X.M., Zhao, W.X., and Hou, G.G., 1998, Very low-grade metamorphism and its geodynamical signification of Triassic strata within the Youjiang River basin: Scientia Geologica Sinica, v. 33, p. 395–405 (in Chinese with English abs.).

Takenouchi, S., and Kennedy, A.C., 1964, The binary system H_2O-CO_2 at high temperatures and pressures: American Journal of Science, v. 262, p. 1055–1074.

Tao, C.G., Liu, J.S., and Dan, G., 1987, Geological characteristics and genesis of Yata gold deposit, Ceheng county: Guizhou Geology, v. 4, p. 135–150 (in Chinese).

Thiéry, R., Vidal, J., and Dubessy, J., 1994, Phase equilibria modelling applied to fluid inclusions: liquid-vapor equilibria and calculation of the molar volume in the CO_2-CH_4-N_2 system: Geochimica et Cosmochimica Acta, v. 58, p. 1073– 1082.

Tödheide, K., and Franck, E.U., 1963, Das Zweiphasengebiet und die kritische Kurve im System Kohlendioxid-Wasser bis zu Drucken von 3500 bar: Zeitschrift für Physkalisoche Chemie Neue Folge, v. 37, p. 387–401.

Wang, Y.G., Wang, L.T., Zhang, M.F., and Wang, L.L., 1995, Texture of the Upper crust and pattern of the disseminated gold deposits distributed in Nanpanjiang area: Guizhou Geology, v. 12, p. 91–183 (in Chinese with English abs.).

Xia, Y., 2005, Characteristics and model for Shuiyindong gold deposit in southwestern Guizhou, China: Unpublished Ph.D. thesis, Guiyang, China, Institute of geochemistry, Chinese Academy of Sciences (in Chinese with English abs.).

Ye, X.X., Wan, G.Q., Sun, Z.Y., Liu, Y.K., Zhou, L.D., Liu, S.R., Xue, D.J., Rivers, L., and Jones, K.W., 1994, Microbeam analysis of gold in Carlin-type gold deposits, southwestern Guizhou, China: Science in China (series B), v. 24, p. 883–889 (in Chinese).

Zhang, F., and Yang, K.Y., 1993, A fission track dating study of the mineralization of the micro-disseminated gold deposit in southwestern Guizhou: Chinese Science Bulletin, v. 17, p. 1593–1595 (in Chinese).

Zhang, H.T., Su, W.C., Tian, J.J., Liu, Y.P., Liu, J.Z., and Liu, C.Q., 2008, The occurrence of gold at Shuiyindong Carlin-type gold deposit, Guizhou: Acta Mineralogica Sinica, v. 28, p. 17–24 (in Chinese with English abs.).

Zhang, X.C., Spiro, B., Halls, C., Stanley, C., and Yang, K.Y., 2003, Sediment-hosted disseminated gold deposits in southwest Guizhou, PRC: Their geological setting and origin in relation to mineralogical, fluid inclusion, and stable-isotope characteristics: International Geology Review, v. 45, p. 407–470.

Zhang, X.C., Hofstra, A.H., Hu, R.Z., Emsbo, P., Su, W.C., and Ridley, W.I., 2005, Geochemistry and $\delta^{34}S$ of ores and ore stage iron sulfides in Carlin-type gold deposits, Dian-Qian-Gui area, China: Implications for ore genesis, *in* Mao J.W., and Bierlein F.P., eds., Mineral deposits research: Meeting the global challenge: Heidelberg, Springer-Verlag, v. 2, p. 1107–1110.

APPENDIX

Element Concentrations in Fluid Inclusions in the Different Stage Quartz at Shuiyindong and Yata

Sample no.	Inclusion no.	Salinity (wt % NaCl equiv)	B (μg/g)	Na (μg/g)	Mg (μg/g)	K (μg/g)	Mn (μg/g)	Fe (μg/g)	Cu (μg/g)	Zn (μg/g)	As (μg/g)	Sr (μg/g)	Ag (μg/g)	Sb (μg/g)	Cs (μg/g)	Au (3σ) (μg/g)	Au (1σ) (μg/g)	Pb (μg/g)	U (μg/g)
SYD035-Q2	mc02b03	6.9	1060	26800	<40	620	<20	<320	<20	<30	30	220	<2	<5	10	<1.7	<0.6	<2	1
	mc02b04	6.9	1040	26800	<60	620	<30	<440	<20	<50	<40	220	<3	<7	30	<2.5	<0.8	5	1
	mc02b05	6.7	1230	26200	<160	810	<110	<1330	50	<140	110	280	20	<30	10	<6.4	3.3	<10	<1
	mc02b07	6.6	1110	25700	<130	680	<100	<1170	<40	<110	<90	180	<10	20	9	<6.6	4.4	<10	<2
	mc02b09	6.9	820	26700	60	940	<70	<720	<40	<50	<80	250	<7	<10	20	<3.9	<1.3	<7	<1
	mc02b10	6.7	1110	26300	<80	690	<70	<1200	<20	<80	80	220	<5	<10	10	<3.1	<1.1	<9	<1
SYD035-Q1	mc02a08	5.4	790	21000	260	410	<40	<540	30	<50	<40	160	5	<7	10	<2.3	<0.8	<4	<1
	mc02a09	5.3	720	20300	150	930	<100	<1610	150	<180	<120	180	20	<20	20	<6.8	<2.3	<10	<2
	mc02a10	5.1	1060	20200	<90	420	<70	<1010	<50	<100	<70	170	<6	<20	20	<4.8	<1.6	<10	<2
	mc02a11	5.3	390	20500	<70	290	<40	<370	<30	<40	90	140	<3	<9	7	<1.6	<0.6	<5	<1
	mc02a12	5.3	870	20600	<40	150	<30	<240	<20	<30	110	170	<2	<6	10	<1.2	<0.4	<3	<1
	mc02a13	5.3	970	20600	<90	270	<60	<820	<30	<90	<70	120	<8	<10	7	<5.4	<1.8	<8	<1
	mc02a14	5.3	530	20700	<40	<140	<50	<630	<40	<70	<60	50	<6	<10	5	<4.2	<1.4	<6	<3
	mc02a15	5.3	640	20600	<100	210	70	<840	<30	<70	<70	170	<6	<10	20	<3.8	<1.3	<6	<1
	mc02a17	5.3	900	20600	<60	300	<40	<430	50	<60	70	140	<2	<9	8	<1.8	<0.6	<5	<1
Q64	mc02c03	5.6	360	21500	<220	410	<120	<1360	70	200	200	30	30	<30	10	6.0	6.0	<20	4
	mc02c05	5.7	500	21600	<120	820	<130	<1480	<110	<150	<150	30	<20	<40	5	<8.7	<2.9	<20	<2
	mc02c06	5.7	1260	21800	<260	<490	<200	<2530	100	<280	340	50	<20	<50	10	<14.3	7.8	40	<3
	mc02c07	5.6	540	21700	<40	340	<30	<410	<10	<40	90	20	9	20	20	3.3	3.3	20	8
YT-5	mc03a06	2.0	250	7700	<20	380	<20	<260	<10	<40	170	1	<2	<5	3	<1.7	<0.6	<2	<1
	mc03a07	2.0	130	7800	<10	180	<10	<70	<10	<10	120	40	<1	<1	4	<0.5	<0.2	<1	<1
	mc03a09	2.0	150	7800	10	140	<10	<130	<10	<10	40	10	<1	<2	1	0.6	0.6	<1	<1
	mc03a10	2.0	270	7800	<10	200	<10	<40	<10	<10	80	3	<1	5	5	<0.2	0.2	1	<1
	mc03a11	2.0	570	7800	<10	310	<10	<140	<10	<10	270	4	<1	20	4	<0.9	0.4	<1	<1
	mc03a12	2.0	250	7900	<40	<90	<30	<470	<10	<60	200	1	<6	20	2	<2.5	<0.8	<5	<1
	mc03a13	2.0	350	7900	<10	50	<10	<190	<10	<20	170	6	<1	<3	5	<0.9	<0.3	<1	<1
	mc03a14	2.0	310	7800	<20	320	<10	<150	<10	<20	150	3	<1	<3	6	0.6	0.6	<1	<1
	mc03a15	2.0	350	7700	<20	350	<10	<100	<10	<10	140	2	1	<3	5	<0.6	0.3	<1	<1
	mc03a16	2.0	290	6900	200	2460	<10	<110	<10	<10	100	3	<1	<2	10	<0.6	0.2	<1	<1
	mc03a17	2.0	450	7800	<10	100	<10	<100	<10	<10	140	2	<1	<2	9	<0.5	0.2	<1	<1
	mc03b03	2.0	330	7800	<70	140	<40	<600	<30	<50	80	3	<6	<10	5	<1.6	0.8	<5	<1
	mc03b04	2.0	210	7700	<30	340	<10	<180	<10	<20	80	5	<1	<3	4	<0.6	0.3	<2	<1
	mc03b06	2.0	330	7700	<10	490	<10	<70	<10	<10	80	3	<1	<1	7	<0.3	<0.1	<1	<1
	mc03b07	2.0	250	7700	<20	<20	<10	<120	<10	<10	70	2	<1	2	2	<0.7	<0.2	<1	<1
	mc03b08	2.0	260	7600	<10	610	<10	<100	10	<10	90	2	<1	2	3	<0.2	0.1	<1	<1
	mc03b09	2.0	350	7800	<30	80	<20	<390	<40	<30	160	1	<2	<4	4	<1.3	<0.5	<4	<1
	mc03b11	2.0	270	7800	<20	160	<10	<190	<10	<20	100	2	<1	<3	5	<0.7	<0.2	<2	<1
	mc03b12	2.0	290	7900	<10	30	<10	<120	<10	<10	110	2	<1	<2	4	<0.5	<0.2	<1	<1
	mc03b13	2.0	210	7700	<20	550	<10	<130	<10	<10	70	2	<1	2	5	<0.6	<0.2	<1	<1
	mc03b14	2.0	260	7800	10	220	<10	<40	<10	10	70	2	1	<1	5	0.3	0.3	<1	<1
	mc03b15	2.0	400	7800	<10	50	<10	<40	2	<10	160	2	<1	2	7	<0.2	<0.1	<1	<1
	mc03b16	2.0	410	7700	<10	480	<10	<60	<10	<10	170	1	<1	<1	7	<0.2	<0.1	<1	<1

APPENDIX *(Cont.)*

Sample no.	Inclusion no.	Salinity (wt % NaCl equiv)	B (μg/g)	Na (μg/g)	Mg (μg/g)	K (μg/g)	Mn (μg/g)	Fe (μg/g)	Cu (μg/g)	Zn (μg/g)	As (μg/g)	Sr (μg/g)	Ag (μg/g)	Sb (μg/g)	Cs (μg/g)	Au (3σ) (μg/g)	Au (1σ) (μg/g)	Pb (μg/g)	U (μg/g)
YT1-012	mc02c14	1.2	190	4800	30	<80	<30	<320	<10	<30	50	4	<4	<10	<1	<2.4	<0.8	<4	<1
	mc02c11	1.0	420	3900	<180	<450	<190	<2380	200	<220	480	10	16	140	<3	<11.6	<3.9	27	<2
	mc02c12	0.8	<200	3200	<120	290	<130	<1820	<110	<150	<130	<4	19	<30	2	<5.6	<1.9	23	8
	mc02c13	0.8	<330	1900	<190	3040	<200	<1860	<90	<220	<190	7	24	60	24	<7.7	4.3	<22	<5
	mc02c16	1.0	130	4000	<70	140	<30	<450	<20	<50	150	2	3	30	1	<2.4	<0.8	<3	1
	mc02c17	1.2	220	4400	<270	<300	<110	<1560	<70	<130	220	<5	<20	70	<3	<5.6	<1.9	<15	<3
	mc02c15	0.8	<200	3000	<100	<270	<110	<1150	<70	<150	420	<4	<6	160	1	<5.3	<1.8	<12	<1
	mc02c18	1.2	<210	4100	<240	990	<90	<1020	<90	<110	200	<4	<7	<20	3	<3.9	<1.3	<9	<3
YT1-010	mc02e03	0.8	110	3200	<50	<90	<20	230	<20	<30	<30	20	<5	<10	17	<2.1	<0.7	8	<1
	mc02e04	0.8	80	3300	<10	40	<10	<60	<10	<10	40	4	<1	4	1	<0.3	<0.1	<1	1
	mc02e05	0.8	80	3100	<20	540	<10	<130	<10	<10	460	8	<2	10	3	<0.6	<0.2	<2	1
	mc02e07	0.8	160	3200	<40	280	<30	<360	<30	<30	80	4	<3	10	3	<1.0	<0.3	<3	<1
YT1-013	mc02e10	0.6	130	2400	<30	140	<20	<250	<10	<20	20	<1	<2	5	<1	<0.9	<0.3	<2	<1
	mc02e11	0.6	70	2500	<80	<60	<30	<410	<20	<30	50	<2	<2	10	1	<1.7	<0.6	<3	<1
	mc02e12	0.6	180	2400	<50	<80	<30	<360	<30	<40	120	1	<7	10	1	<1.2	<0.4	<3	<1
	mc02e13	0.6	100	2500	<60	<110	<40	<480	<20	<60	<40	<3	<7	10	3	<3.3	<1.1	<5	<1
YT-4	mc02a04[1]	11.1	<4870	41300	<1950	<5680	<1990	<28130	<1420	<2950	<2250	<70	<220	<400	<20	<65	<22	<240	<30
	mc02a05[1]	11.1	<2180	43600	<1200	<3080	<960	<16000	<570	<1390	1880	<40	<140	340	<20	<57	<19	<140	<20
	mc02a06[1]	11.1	<7810	43600	<6170	<11450	<3980	<55880	<2850	<5460	<3950	<130	<240	<950	<80	<600	<200	<480	<50
	mc02c08	11.1	1060	43400	<190	<550	<210	<3000	<130	<290	<240	50	<30	<40	<3	<9	<3	<20	4

Notes: < values show the limit of detection (LOD) at 3σ; detection limit of elements (3δ): B ~80, Na ~10, Mg ~30, K ~80, Mn ~20, Fe ~400, Cu ~40, Zn ~30, As ~20, Sr ~1, Ag ~2, Sb ~5, Cs ~1, Au ~1, Pb ~4 and U ~1 μg/g, respectively

[1] Vapor-rich inclusions